Marine Geology 488 (2025) 107609

Contents lists available at ScienceDirect

Marine Geology

journal homepage: www.elsevier.com/locate/margo

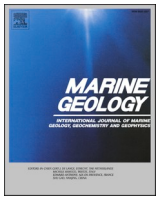

Research Article

Quantitative structural geology in the deep ocean using photogrammetry: Implications for the polyphased tectonic evolution of the Buteur Ridge, French Guiana

Charline Coudun [a,*], Paul Brichard [b], Christophe Basile [a], Sébastien Zaragosi [b], Vincent Marieu [b], Martin Patriat [c], Lies Loncke [d]

[a] Univ. Grenoble Alpes, Univ. Savoie Mont Blanc, CNRS, IRD, Univ. Gustave Eiffel, ISTerre, 38000 Grenoble, France
[b] Univ. Bordeaux, CNRS, Bordeaux INP, EPOC, UMR 5805, F-33600 Pessac, France
[c] Univ. Brest, CNRS, Ifremer, Geo-Ocean, F-29280 Plouzané, France
[d] University of Perpignan Via Domitia, Centre de Formation et de Recherche sur les Environnements Méditerranéens (CEFREM), UMR 5110, 52 Avenue Paul Alduy, 66100 Perpignan, France

ARTICLE INFO

Editor: Michele Rebesco

Keywords:
Underwater photogrammetry
3D reconstruction
Nautile submarine
Structural geology
Sedimentology
Post-rift unconformity
Buteur Ridge

ABSTRACT

The Buteur Ridge is a 7 km-long and 6 km-wide relief on the eastern rifted margin of the Demerara Plateau, offshore French Guiana. This margin was formed during the Lower Cretaceous. In early 2023, the oceanographic cruise DIADEM used a manned deep submersible (*Nautile*) to sample and directly observe the eastern flank of this 3750 m-deep ridge.

This study presents a new underwater photogrammetric method developed from the *Nautile* video records. This method incorporates both camera and submarine movements to produce photogrammetric 3D models of the seafloor below decimetre scale. The presented underwater photogrammetric method can be used for both past and future video records, as long as both underwater device and camera movements are recorded.

The data obtained from the 3D reconstructions allow to reconstruct detailed stratigraphic and structural framework of the Buteur Ridge. The eastern flank of the Buteur Ridge is entirely composed of sedimentary layers. Structural analysis at bed scale suggests prograding structures likely associated with a N-S-directed paleocurrent. At ridge scale, structural analysis combined with seismic observations suggests that the Buteur Ridge is the result of a polyphased tectonic evolution. We highlight that Cretaceous tilted blocks, bounded by east-dipping faults, are overlapped by a post-rift unit. The syn-rift units are in contact with the east-dipping post-rift unit by a post-rift unconformity. Subsequent tilt and fault reactivation offset both the post-rift unconformity and the post-rift unit, resulting in the present relief of the Buteur Ridge.

1. Introduction

3D imaging of the seafloor is compulsory to understand difficult-to-access deep environments. With the development of imaging techniques, we gained new knowledge in many fields (e.g., geology, biology, archaeology). However, providing a detailed geological study on deep water outcrops has always been challenging. Seismic imagery is widely used to describe these structures but only gives large scale (kilometres to tens of kilometres) and generally 2D information. In order to obtain direct observations and structural measurements on a decametric or even metric scale, the use of AUV (Autonomous Underwater Vehicles), ROV (Remotely Operated Vehicles) or manned submarines offers a solution. These cameras-equipped devices image the seabed and allow making accurate in situ observations. Structural measurements (orientations: dip angle, dip direction; scales of structures) are required to characterise the outcrops. Unfortunately, these measurements are limited at such depths due to: (i) the lack of tools for direct measurements; (ii) the lack of visibility in deep-sea environments. The rare structural measurements are visually estimated. They are therefore imprecise. Hence, the development of new methods is essential to

* Corresponding author.
E-mail addresses: charline.coudun@univ-grenoble-alpes.fr (C. Coudun), paul.brichard.pro@gmail.com (P. Brichard), christophe.basile@univ-grenoble-alpes.fr (C. Basile), sebastien.zaragosi@u-bordeaux.fr (S. Zaragosi), vincent.marieu@u-bordeaux.fr (V. Marieu), martin.patriat@ifremer.fr (M. Patriat), lies.loncke@univ-perp.fr (L. Loncke).

https://doi.org/10.1016/j.margeo.2025.107609
Received 1 November 2024; Received in revised form 13 June 2025; Accepted 19 June 2025
Available online 20 June 2025

improve geological studies in the deep-sea.

Over the years, the use of aerial digital photogrammetric cameras became widespread and both algorithms and softwares were improved (e.g., Jiménez-Jiménez et al., 2021; Luhmann et al., 2015; Mozas-Calvache et al., 2012; Serifoglu Yilmaz and Gungor, 2016; Serifoglu Yilmaz et al., 2018; Sona et al., 2014; Svennevig et al., 2015; Westoby et al., 2012; Zhou et al., 2019). Aerial photogrammetry is now used routinely onshore in order to provide three-dimensional (3D) reconstructions of outcrops in several fields in sedimentology (Chesley et al., 2017), paleoseismology (Bemis et al., 2014), coastal environments (Gonçalves and Henriques, 2015; Ventura et al., 2018), glaciers (Ryan et al., 2015), mining (Honarmand and Shahriari, 2021), deformed domains (Sangsrichan et al., 2023; Liang et al., 2023; Peace and Jess, 2023; Vollgger and Cruden, 2016) or general areas surveys (Śledź et al., 2021). In comparison, underwater photogrammetry is less used due to the complexity of deep-sea outcrops access, to difficulty of lighting and to movements of the sedimentary particles and water masses. Recent articles have demonstrated the feasibility of deep-sea photogrammetry using AUV and ROV (Arnaubec et al., 2023; Escartín et al., 2016; Ferrera et al., 2023; Flores and ten Brink, 2024; Garcia et al., 2017; Gerdes et al., 2019; Kwasnitschka et al., 2013; ten Brink et al., 2023; ten Brink et al., 2024). However, the use of photogrammetry in the marine environment, using a single camera that records continuously, has only been applied to ROVs and AUVs and has not yet been developed for deep manned dives.

In 2023, the DIADEM (Basile and Loncke, 2023) cruise was carried out on board the French oceanographic vessel *Pourquoi Pas?*. The manned submarine *Nautile* was used to observe and sample in situ outcrops of the Demerara Plateau in order to reconstruct their tectonic and stratigraphic history. The *Nautile* has three cameras recording continuously during the dives: one immobile at the bottom of the *Nautile* and two mobile front cameras. The cumulative movements of both front cameras and the submarine itself, lead to the impossibility to apply conventional photogrammetric techniques used for fixed cameras.

The aim of this paper is therefore to:

(i) Provide a new photogrammetric method applied to the *Nautile* submarine which includes the movements of the cameras and the submarine to produce photogrammetric derived images of the seafloor.
(ii) Demonstrate the robustness of this method for structural measurements.
(iii) Provide a geological study of a deep-sea outcrop (the Buteur Ridge) located on the Demerara Plateau using the photogrammetric data obtained from the *Nautile* submarine.

2. Study site

The Demerara Plateau is a submarine bathymetric high, 230 km long and 170 km wide, lying between 1000 and 3000 m depth, and located north of French Guiana and Suriname shelves (inset Fig. 1A). It is bordered by both the Jurassic Central Atlantic and Cretaceous Equatorial Atlantic oceans (Basile et al., 2013; Gouyet, 1988; Graindorge et al., 2022; Loncke et al., 2020; Loparev et al., 2021; Mercier De Lépinay et al., 2016). The eastern margin of the Demerara Plateau is a rifted margin formed during the lower Cretaceous (Basile et al., 2005; Basile et al., 2013; Basile et al., 2022; Campan, 1995; Gouyet, 1988; Greenroyd et al., 2008; Loncke et al., 2022; Mercier De Lépinay et al., 2016; Museur et al., 2021; Nemčok et al., 2015). The Buteur Ridge is a 7 km-long, 6 km-wide relief located at the transition between this margin and the abyssal plain (or the Amazon deep-sea fan) (Fig. 1A, B). Due to its location, the Buteur Ridge is one of the few sites where tectonic and sedimentary records of the Equatorial Atlantic rifting are outcropping, making it a kea area. It has been previously identified from GUYAPLAC bathymetric survey (Le Suave and Beuzart, 2003) and surveyed during several scientific cruises. Vertical and wide-angle seismic profiles from the IGUANES (Loncke, 2013) (Fig. 1C) and MARGATS (Graindorge and Klingelhoefer, 2016) cruises show that the 3750 m-deep Buteur Ridge is an acoustic basement ridge delimited on its western side by a normal fault (Basile et al., 2022; Girault et al., 2023; Graindorge et al., 2022; Museur et al., 2021). In 2016, the DRADEM cruise (Basile, 2016) dredged the rocks outcropping on the sea floor, retrieving a single azoic coarse-grained block of sandstone (Girault et al., 2023).

In early 2023, the oceanographic cruise DIADEM took place at the same site, using a manned deep underwater submarine (*Nautile*). Manned deep underwater dive is commonly used to directly observe the seafloor, and to allow the selection of sampling location. In fact, eight sandstones were sampled during the underwater dive on the eastern slope of the Buteur Ridge. This dive also provided six hours of video recording on each of the three *Nautile* cameras.

3. Material and methods

Photogrammetry is based on the principle of triangulation by detecting homologous points in a series of photographs (Wang, 1998). Several vector computations estimate the position of homologous points in a three-dimensional space (Li et al., 1997). 3D reconstructions derived from a single camera, without navigation data, only provide relative information regarding size, orientation, and position (e.g., Arnaubec et al., 2023; Hartley and Zisserman, 2004). To achieve accurate scaling and correct positioning for absolute measurements in 3D reconstructions, the integration of external data is essential. Scene scaling can be accomplished by using known object dimensions. However, navigation data is indispensable for georeferencing the photogrammetric results. As navigation data enables both the scaling and georeferencing of the photogrammetric reconstructions (e.g., Arnaubec et al., 2023), we used it in this study. Additionally, this data includes information on the geographical position of the camera (from the *Nautile* itself), as well as the camera's orientation.

All recordings used for 3D reconstructions were captured using IP Apex SeaCam[1] cameras, equipped with a 3.9 mm to 46.8 mm, f/1.8 to f/2.0 lens featuring a focus range from approximately 110 mm to infinity. The image sensor is a 1/2.3" CMOS and we used full HD mode with a resolution of 1920 × 1080 pixels, corresponding to a 16:9 aspect ratio. The outcrops were lit using a system of six V Light[2] panels.

3.1. Field data acquisition

3.1.1. Nautile position

The position of the *Nautile* is known by two methods:

(i) USBL (Ultra-Short BaseLine, *Posidonia 2 Ixblue*) consists of a transceiver mounted under the support vessel (*Pourquoi Pas?*) and a transponder mounted on the *Nautile*. The USBL system converts the two-way travel time of an acoustic pulse between the transceiver and the transponder into a distance. The signal is then received by the transceiver's four receivers. The next step is decoding and processing to determine the direction and distance of the transponder from the transceiver. The direction of the signal is obtained by exploiting the phase differences between the four receivers (interferometric technique). Using the GNSS position of the *Pourquoi Pas?*, information on its roll, pitch and heading, and the velocity profile of seawater (to correct the velocity of sound waves), the system derives the position of the *Nautile*: latitude, longitude, depth. Measurement errors are of the

[1] https://www.deepsea.com/product-documentation/cameras/ip-apex-seacam/#ip-apex-seacam (accessed on 23 April 2025)
[2] https://www.teledynemarine.com/en-us/products/Pages/led-v-series.aspx (accessed on 23 April 2025)

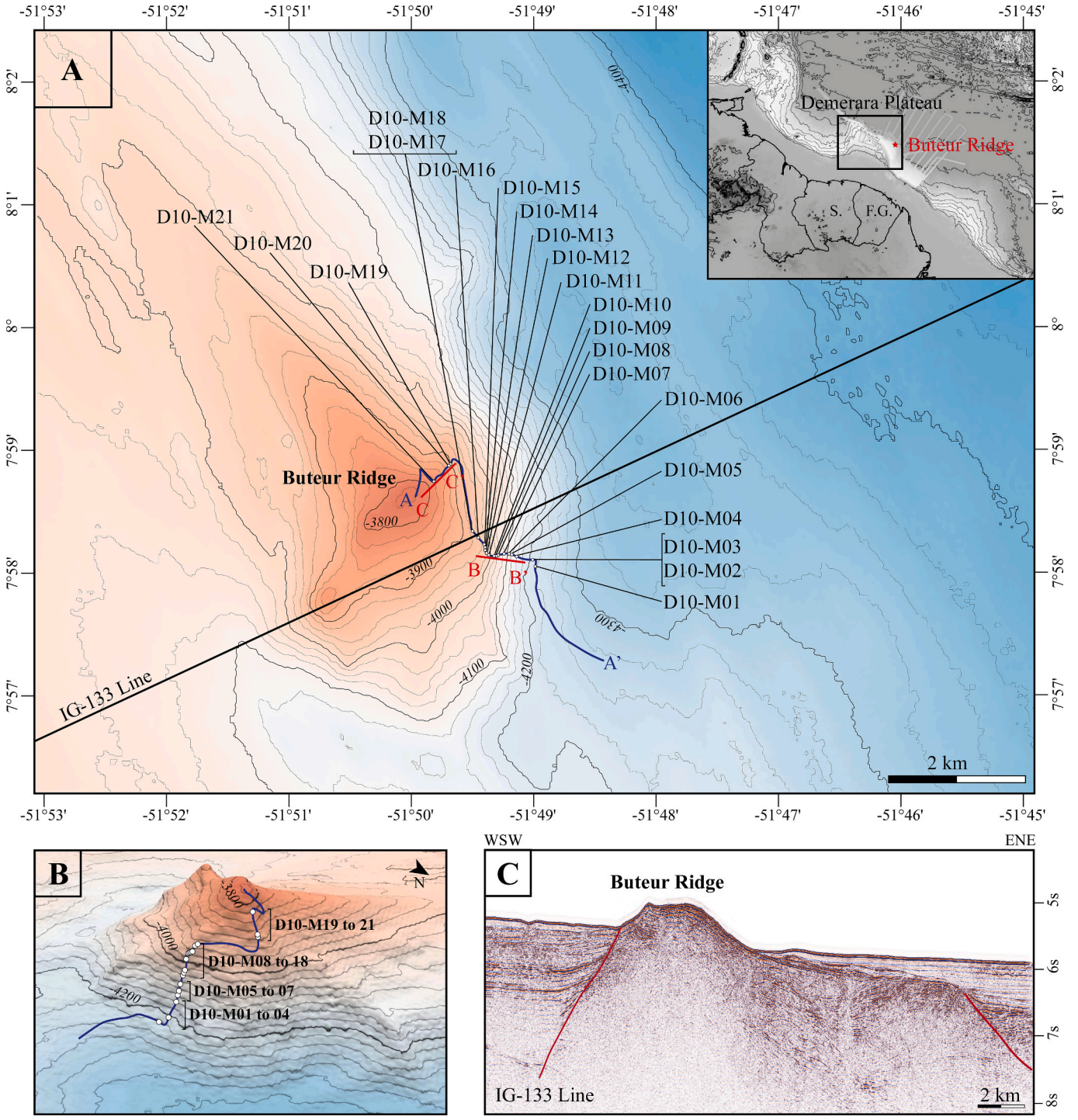

Fig. 1. (A): Topographic map of the Buteur Ridge (background from the IGUANES, DRADEM and MARGATS cruises: Loncke, 2013; Graindorge and Klingelhoefer, 2016; Basile, 2016). Isobaths every 25 m. Line AA' indicates the location of the *Nautile* dive path, the topographic profile is shown in Fig. 13. Lines BB' and CC' indicate the location of the cross-sections shown in Fig. 14. 3D models are named with the prefix D10-M. (B): 3D visualisation of the topography of the eastern face of the Buteur Ridge. The 3D models are located along the AA' line. (C): Seismic line IG-133 from IGUANES cruise (Loncke, 2013). Vertical exaggeration: 4.1. Normal faults are indicated by the red lines. (For interpretation of the references to colour in this figure legend, the reader is referred to the web version of this article.)

order of 0.5 % of the water depth, which corresponds to a decametric accuracy for depths between 4200 m and 3750 m.

(ii) INS (Inertial Navigation System, *Phins Surface Ixblue*) coupled to an LBL (Long BaseLine, *Ramses Ixblue*) providing position, true heading, speed, depth, rotational and translational movements with decimetric accuracy but in a local reference frame. The drift of the INS is corrected every fifteen minutes by the X and Y positioning provided by the USBL.

Depth is also recorded by a pressure sensor mounted on the *Nautile*. Data are recorded continuously throughout the dive. The quality and limitations of the available navigation data are crucial factors influencing the accuracy of scaling, orientation, and overall positioning of the resulting 3D models (e.g., Arnaubec et al., 2023). Consequently, our study employs navigation data from the INS, coupled with LBL, which offers greater accuracy than the commonly used USBL. This data is further corrected with USBL information to mitigate drift.

3.1.2. Nautile movements

The INS system measures both the rotational and translational movements of the *Nautile*. The rotational motions (Fig. 2A) include yaw, roll and pitch, corresponding to the rotation around the *Nautile*'s vertical axis (Z axis) (i.e., rotation relative to the north), longitudinal axis (X axis) (i.e., tilted right or left apart from the horizontal) and transverse axis (Y axis), (i.e., forward and backward rotation), respectively.

The translational motions include surge, sway and heave. These motions are provided in X and Y by the INS system and in Z by the pressure sensor, but are insignificant in deep water due to the stability of the water mass.

3.1.3. Camera movements

The *Nautile* has three cameras recording continuously, one camera recording vertically and the two others horizontally (Fig. 2A). Only the vertical camera and the port side horizontal camera are connected to the INS system and can be used in the photogrammetric process.

The vertical camera is fixed perpendicularly to the *Nautile* and facing downwards (Fig. 2B), in the same configuration as the airborne cameras (aircraft or drone) commonly used in photogrammetry. In this way, the vertical camera captures images in conditions that are optimal for photogrammetry, limiting angular errors. However, for 3D reconstruction and structural analysis, the horizontal camera (Fig. 2B) is preferred to the vertical one. In fact, in an environment with steep slopes, the vertical camera does not allow large areas to be video recorded with a good light quality. In addition, the vertical camera is more sensitive to the effects of turbidity caused by the navigation of the *Nautile* close to the seabed sediments.

The horizontal camera records the lens change in tilt (rotation around Y axis) and pan (rotation around Z axis) (Fig. 2C). All motion data is recorded and synchronised at a frequency of 1 Hz. This camera always records in HD quality, but switches to 4 K quality when sampling occurs.

3.2. Combination of Nautile and camera movements

Combining the rotation of the *Nautile* (yaw, roll and pitch, Fig. 2A) with the rotation of the camera (tilt and pan, Fig. 2C) allows the position and strike of the lens to be geographically determined and used for each shot. For the calculated angles, we determine a final pitch, roll and yaw. The final pitch is obtained by adding the pitch of the *Nautile* to the tilt of the camera plus 90°. The final roll is the *Nautile*'s roll, as the camera has no longitudinal axis movement. The final yaw is given by adding the yaw of the *Nautile* and the pan of the camera.

3.3. Processing workflow

The photogrammetric method, based on the work of Arnaubec et al. (2023) and adapted for the *Nautile*, focuses on the compilation of navigation data (geographical coordinates and depth) and the movements of both the *Nautile* and the camera (Fig. 3). All the pictures used to reconstruct the 3D models are extracted from the videos at a frequency of one image per second, ensuring good overlap and maximising the number of homologous points. We used scripts in conjunction with ImageMagick software © version 7 (ImageMagick Studio, 2018) to convert videos into images and carry out the following pre-processes. Each image was assigned a unique name derived from the corresponding video file name. We then generated a navigation file, using a consistent one-second time increment, to link each image to a distinct navigation point. The extracted images contained burn-in text overlays, which were positioned solely in the top header. These overlays hindered the possibility of 3D reconstructions. To address this, we crop the upper portion of each image containing the header, reducing the image size from 1920 × 1080 pixels to 1920 × 1044 pixels. We used groups of between 50 and 160 images (1–2 min) to construct each 3D model, which represents outcrops no more than fifteen metres in height and width. The cropped pictures, the navigation data and motion data are then imported into the 3D software Agisoft Metashape Professional © version 2.0.0 (Agisoft, 2022), which uses SfM (Structure-from-Motions)

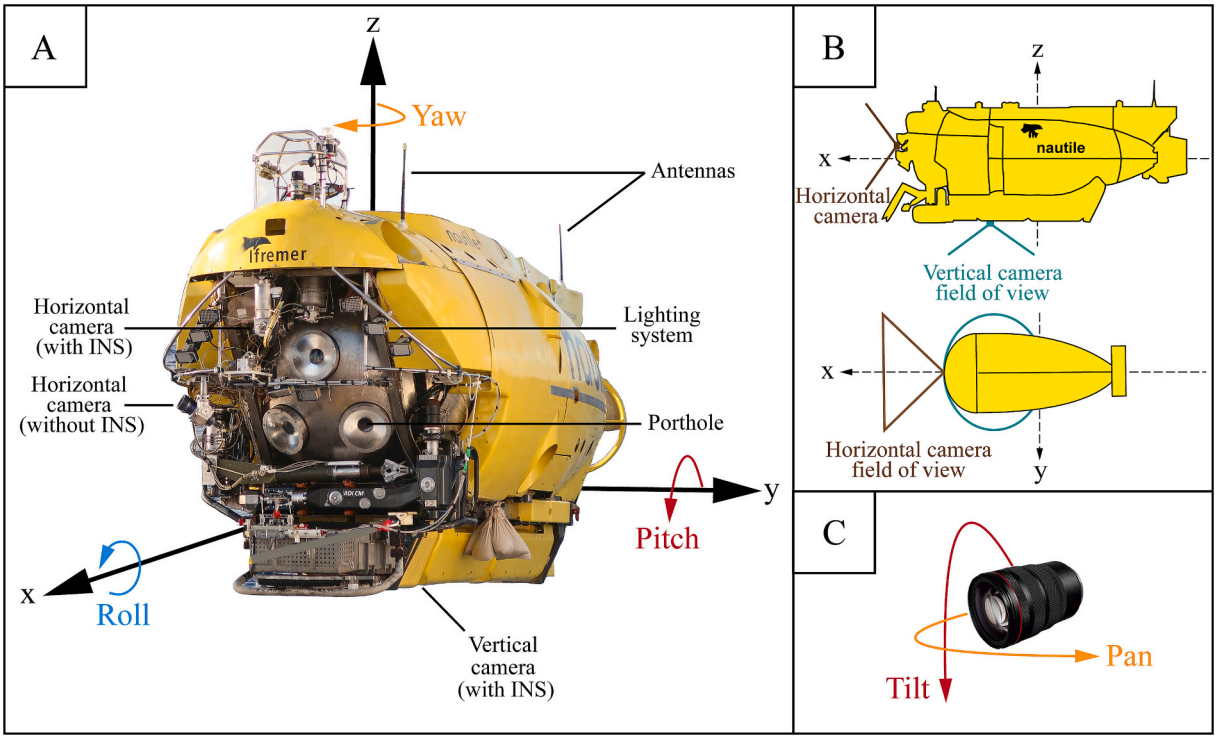

Fig. 2. Illustration of all the movements involved during a *Nautile* dive. (A): *Nautile* rotational movements: Pitch, Yaw and Roll. INS: Inertial Navigation System. (B): Schematic *Nautile* profile and vertical view, camera locations and field of view. (C): Camera movements: Pan and Tilt.

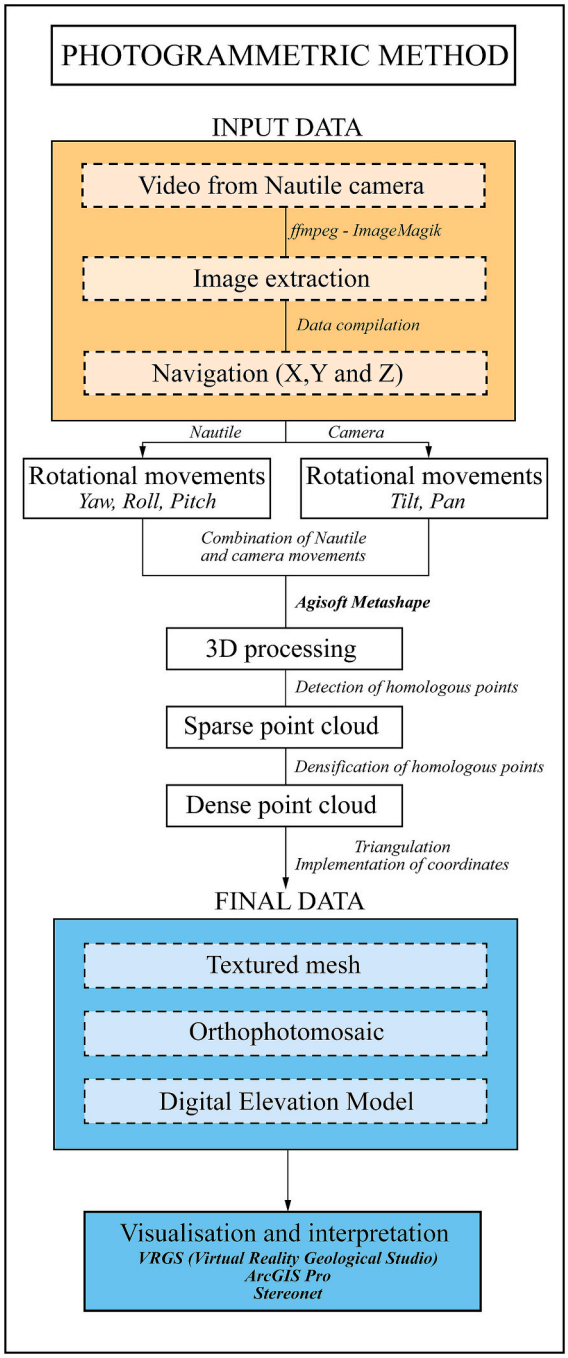

Fig. 3. Flow diagram illustrating the photo-based 3D reconstruction applied to the *Nautile* photogrammetry.

algorithms. The machine processing time is reduced to about fifteen minutes for the hardware set-up used (Central Processing Unit: 2 × Intel Xeon Gold 6240R @2.40GHz 24 cores; Graphics Processing Unit: Nvidia RTX A5000; Ram (GB): 512; Operating System: Ubuntu).

The Agisoft Metashape © software first generates a sparse point cloud and then a dense point cloud (Fig. 4). The sparse point cloud is generated by detecting homologous points between pictures, and the dense point cloud is generated by densifying these points. The triangulation of these points, the generation of the texture and the implementation of the individual point coordinates produce the textured meshes which can then be used as 3D models (Fig. 4). The software also produces orthomosaics and DEMs (Digital Elevation Models) (Fig. 4). The DEM is derived from a digital calculation that produces a vertical view of the model's relief. It allows slopes calculation thanks to detailed bathymetry. An orthomosaic is a geometrically corrected image generated by stitching together multiple photographs, which are processed to correct distortions introduced by the camera angle, altitude, and terrain. This results in a true-to-scale image presented as a vertical panoramic view. It provides a wide view of the outcrop that cannot be seen in a single view from the *Nautile*'s porthole.

3.4. Visualisation and interpretation

The structural geology software Virtual Reality Geological Studio © (VRGS) version 3.1 (VRGeoscience Limited, 2022) was used to import textured models (triangular meshes) and measure the structural parameters.

Stereographic projections were generated using Stereonet software © version 11.6.0 (Allmendinger, 2024). They are presented on the lower hemisphere Schmidt canvas.

The Digital Elevation Models (DEMs) and orthomosaics generated from the 3D mesh models are integrated into the GIS software ArcGIS Pro © version 3.4.3 (Esri, 2025). The UTM 22 N projection is used.

3.4.1. Bedding (S0) measurements

Three methods were used to measure the strike and dip of the stratigraphic surfaces:

(i) The VRGS © bedding tool was used directly. This tool is effective when the stratigraphic surface outcrops, is perfectly flat and shows no accumulation of pelagic sediments. In fact, the accumulation of fine sedimentary particles will distort the bedding surface when the 3D texture meshes are generated. For this reason, the VRGS © bedding tool was only used when the surface was clear of sediments.

(ii) When a single stratigraphic surface edges on outcrop, two non-parallel edges of the stratigraphic surface were used as directional vectors of the stratigraphic plane. The VRGS © plunge tool was used to determine the plunge and azimuth of each line, and these two lines define the orientation of the stratigraphic plane they belong to.

(iii) Finally, using the joint pattern provides an information for the structural parameters of the stratigraphic plane. Joint systems are defined as fractures that form regular networks with constant angles between two or three preferred orientations, and that are often perpendicular to the stratigraphic surface. Each fracture system is relative to only one stratum. When a joint system is clearly identified for a bed, the VRGS © fracture tool was used to determine the dip and azimuth of each joint. Thus, the intersection of projected joint planes of the same joint system should be perpendicular to the adjacent stratigraphic layers.

3.4.2. Thickness of strata and interbeds

The 3D reconstructions highlight the stratigraphic surfaces and provide access to their bases and tops. To determine the thickness of each stratum, we used the length of the vector generated by the VRGS © 3D measurement tool. The plotted vector corresponds to a vector perpendicular to the base and top.

To determine the thickness of the interbeds, which are less competent and therefore more difficult to measure directly with the VRGS © tools, we used the following calculations for the two cases shown in Fig. 5. These cases allow to consider the dip of structures. Eq. (1) is used when the beds tilt towards the *Nautile*. Eq. (2) is used when the beds tilt away from the *Nautile*.

$$z = \sin\left[180 - \left(90 + \cos^{-1}(Z/H) + \alpha\right)\right] \times H \quad (1)$$

$$z = \sin\left[90 - \cos^{-1}(Z/H) + \alpha\right] \times H \quad (2)$$

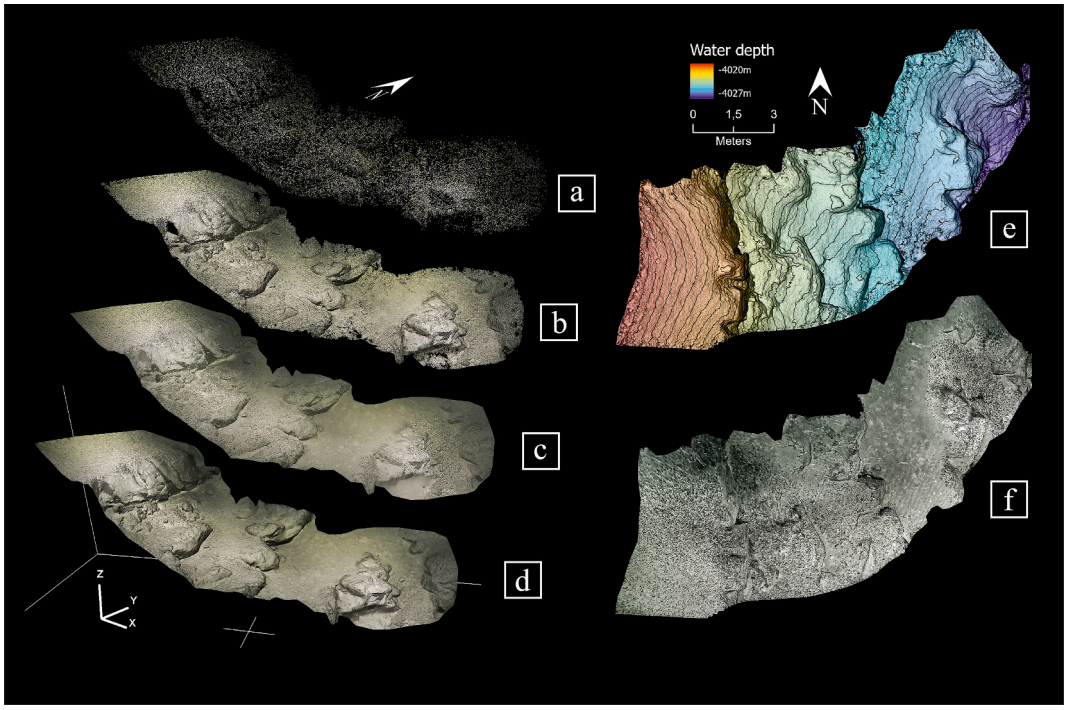

Fig. 4. Example of the different steps for the 3D reconstruction (D10-M10) along the path of the *Nautile*: a. sparse point cloud; b. dense point cloud; c. dense mesh coloured for depth; d. the textured mesh; e. Digital Elevation Model and f. orthophotomosaic. a to d are perspective views, e and f vertical views.

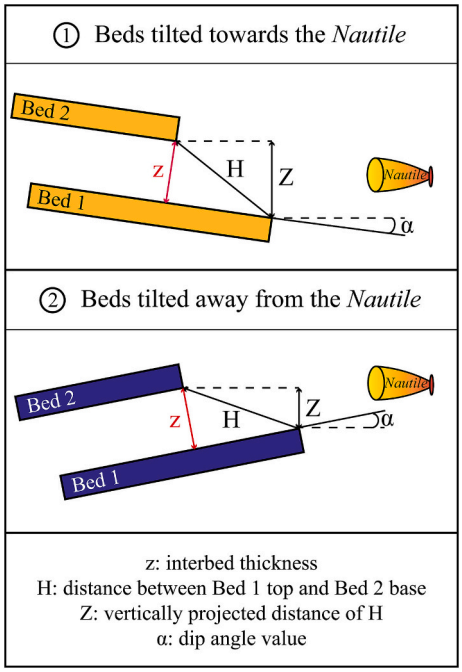

Fig. 5. Geometric parameters used to calculate the interbed thickness depending of the apparent dip of bedding.

Where *z* is the interbed thickness; *H* is the distance between the first bed top and the second bed base; *Z* is the vertically projected distance of *H* and α is the apparent dip angle value.

The H distance is given by the vector length generated by the VRGS © measurement tool. This vector is perpendicular to the top of the first stratum and the base of the second stratum. The Z parameter is given by the difference in Z of this vector measured by the VRGS © software.

3.5. 3D reconstructions robustness

In their 2023 study, Sangsrichan et al. (2023) employed the percentage error as the difference between the actual value of a structural parameter (i.e., measured in the field) and the obtained value (i.e., obtained by the VRGS software ©). It is not feasible to conduct direct measurements on deep-sea outcrops to ascertain the percentage error. To assess the reliability of the 3D reconstructions produced with the integrated correction of the *Nautile* and horizontal camera motions, we conducted a comparison between the structural measurements obtained with the 3D reconstructions generated with the horizontal camera data (Fig. 6A) and the vertical camera data (motionless camera) (Fig. 6B). All the values shown in Fig. 6 are obtained by VRGS © measurements tools.

For each stratification plane, the average angle difference between the 3D reconstructions based on vertical and horizontal camera is less than 5°, which is comparable to the variation in usual field compass measurements. The average percentage error of the distance measurements is 3.3 % which is acceptable.

Finally, it is also essential to consider the angle uncertainty of the model generated during the photogrammetric process. The Agisoft Metashape © software gives the angular error during the alignment of the photographs. For all the 3D reconstructions produced, this error has never exceeded 1°.

4. Results

4.1. Structural analysis of the Buteur Ridge

In this study, twenty-one 3D reconstructions were generated from the Buteur Ridge dive (Fig. 1A, B). These reconstructions represent thirty-two cumulative minutes of video recording, which constitutes 8 % of the total dive time. However, they illustrate 23 % of the vertical outcrop height visible during the dive. The 3D reconstructions presented here illustrate the majority of the geological structures and sedimentary sequences encountered during the dive on the eastern face of the Buteur Ridge (Fig. 1A, B and Fig. 7). All the structural measurements used in

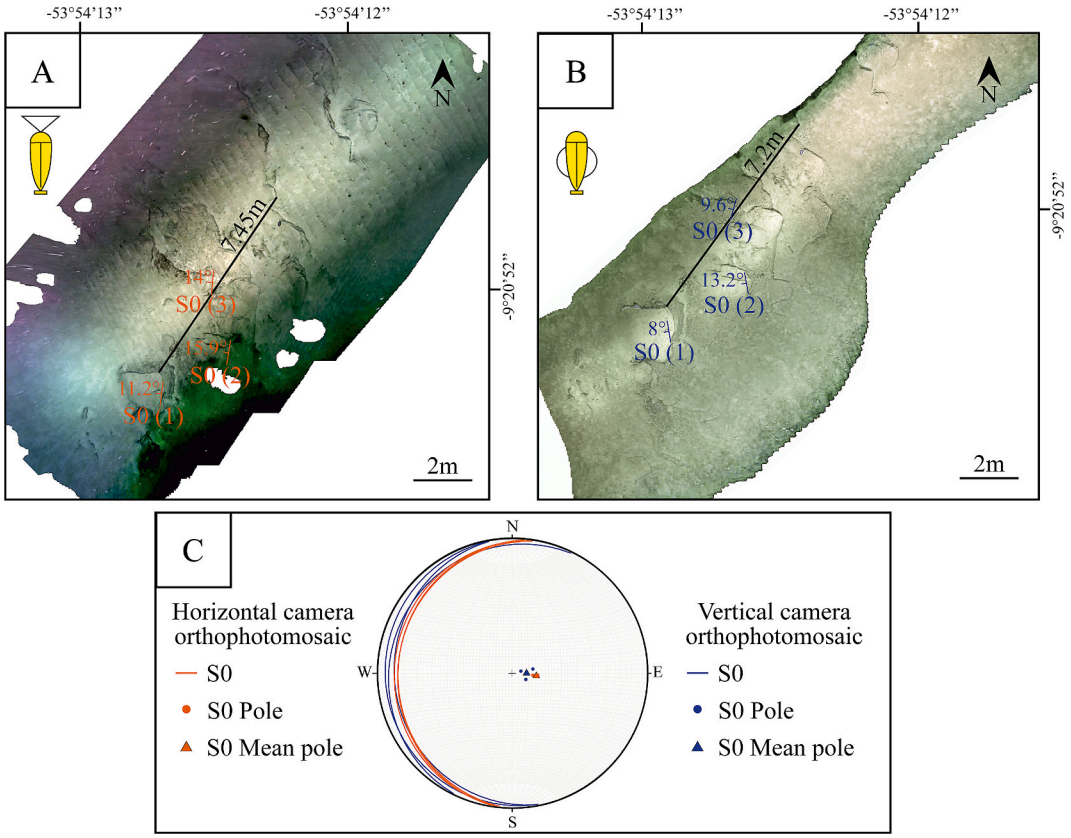

Fig. 6. Example of the comparison of structural parameter values obtained from 3D reconstructions, of the same outcrop, generated from horizontal or vertical camera data. In light of the limitations in acquiring both reliable vertical and horizontal records, the model has been derived from another dive on the Demerara Plateau. (A): Horizontal camera generated orthophotomosaic and location of the measurement areas. (B): Vertical camera generated orthophotomosaic and location of the measurement areas. (C): Dip bed values obtained from identical areas shown on the Schmidt canvas.

this study are summarised in Fig. 8 (structural data compiled in Supplementary Table S1).

Models D10-M01, D10-M02, D10-M03 and D10-M04 did not provide structural or stratigraphic measurements as they illustrate the rockfalls at the bottom of the slope (Fig. 1A, B). They were therefore used to estimate the size of the fallen blocks. Models D10-M16, D10-M17 and D10-M18 did not provide structural measurements but were used to complete the general stratigraphic log of the Buteur Ridge (Fig. 7). However, as the strata in these models were not competent, it was not possible to construct detailed logs of the outcrops. Finally, model D10-M20 does not provide any structural measurements, but is used to construct the log of the outcrop.

4.1.1. Bedding (S0)

We reconstructed the stratigraphic log of the Buteur Ridge from the observations made during the dive complemented by the measurements made on the 3D models (Fig. 7). Only sedimentary strata outcrop along the Buteur Ridge. The most competent sedimentary beds, which are separated by interbeds, are decimetres to multi metres thick. The lithology is predominantly made of sandstones with six sandstone samples collected along the *Nautile* dive, taken directly from the beds (Fig. 7). The depositional environment associated with these sandstones is continental, mainly fluvial. The interbeds were not sampled, but we infer from their competence that they may be finer-grained material, dominated by clay or silt, covered by pelagic deposits.

The stratigraphic sequence of the Buteur Ridge can be divided into three main units based on morphology, orientation and petrography of the sedimentary layers. They are described from the deepest to shallowest unit:

We define a first unit between 4143 and 4075 m below sea level (seafloor depths) (models D10-M05 to D10-M07). These strata are competent, fractured, but show limited lateral continuity (Fig. 9A). They are typically less than a metre thick and separated by several decimetres of interbedding (Fig. 9B). We measured forty-two orientations of S0 on the three 3D models. S0 strike between N10 and N25 and dip between 10° and 13° eastward (Fig. 8 and Fig. 9A). At depths of 4142.9 m and 4092 m, two samples (N3 and N4) were collected (Fig. 7). Sample N3 is a well quartz-cemented very coarse-grained sandstone. Sample N4 is a well quartz-cemented medium-grained sandstone. The strata of the 3D models D10-M05 and D10-M06 are thicker and less weathered compared to the thinner and more crumbled layers of the model D10-M07. We tentatively relate this variation to variability of the grain size.

The second unit ranges between 4059 and 3929 m below sea level. It consists in multi-metre-thick beds, ranging from one to six metres thick, that are separated by very thin interbeds (Fig. 10A, B, C and D). The massive beds, laterally continuous, form overhangs along the slope due to their considerable competence (Fig. 10A). The twenty-nine S0 measurements taken on the seven 3D models indicate an average S0 striking between N10 and N22 for the lower part (Fig. 8 and Fig. 10C) and between N150 and N155 for the upper part (Fig. 8 and Fig. 10A). The average S0 dip ranging from 8° to 15° westward (Fig. 8 and Fig. 10A, C). Sample N5, collected at 4024.9 m depth (Fig. 7), is a coarse-grained sandstone with minimal weathering and corresponds to the lithology of the lower part of this second unit. Sample N9 (3947.5 m, Fig. 7) is a well cemented very fine-grained quartzite, and is representative of the massive beds of the upper part. Both N5 and N9 samples show bedding at millimetre scale.

The third unit is between 3898 m and 3760 m below sea level. The strata show significant alteration. This has resulted in a weathered, hilly surface appearance (Fig. 11A). These layers are between one and two

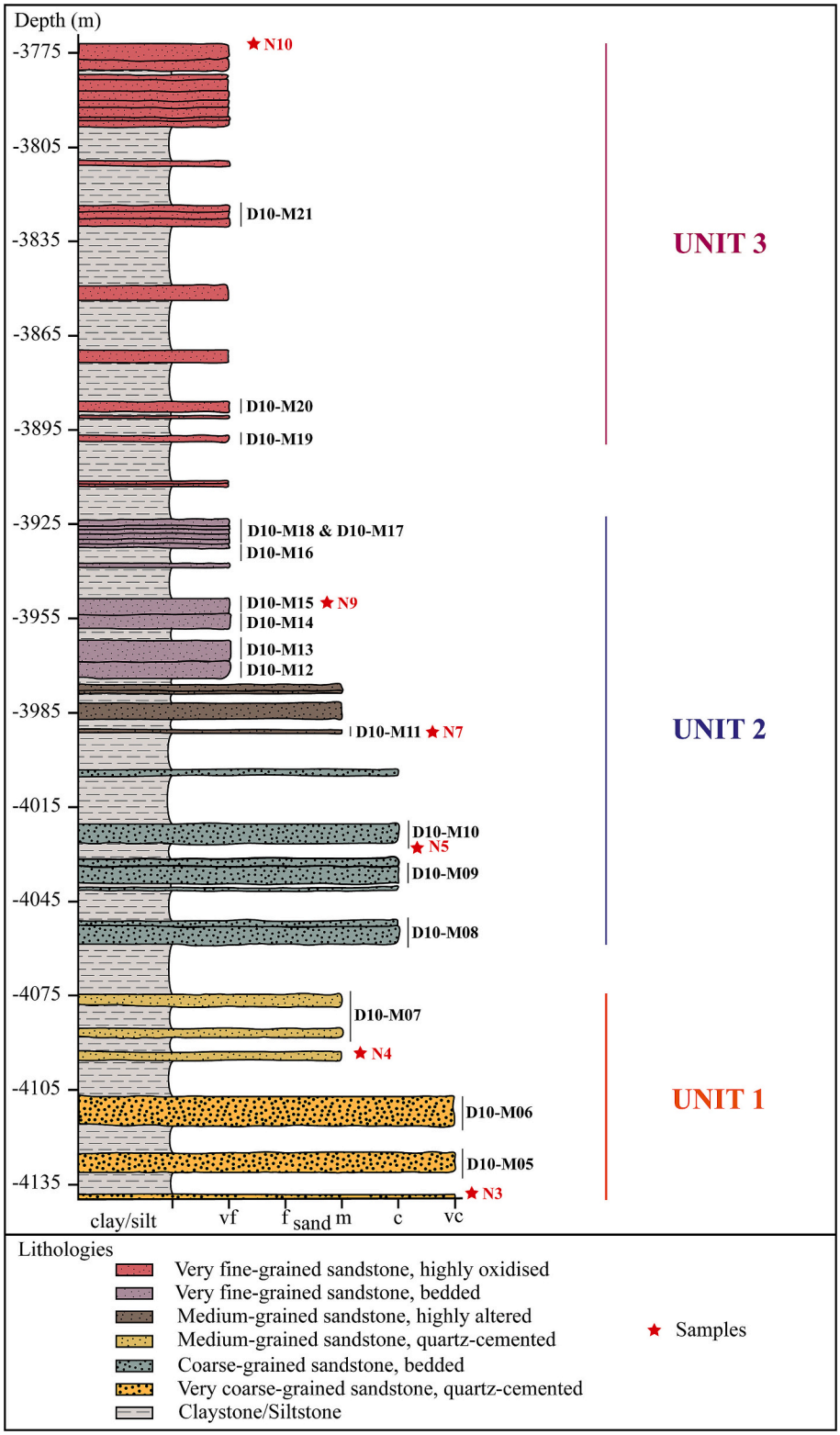

Fig. 7. Stratigraphic log of the eastern slope of the Buteur Ridge with the intervals where photogrammetric models were performed. The red stars indicate the sample locations. (For interpretation of the references to colour in this figure legend, the reader is referred to the web version of this article.)

metres thick and show a lack of competence (Fig. 11B). However, the thickness of the interbeds is limited compared to the first unit. The fifteen S0 measurements taken on the two 3D models show an average S0 between N178-10E and N20-30E (Fig. 8 and Fig. 11A). Sample N10, collected at 3761.7 m depth (Fig. 7), is a very fine-grained and poorly cemented sandstone containing 60 % quartz and showing significant alteration characterised by the presence of iron oxides. This highly oxidised lithology can explain the lack of competence and the weathered appearance of the layers.

4.1.2. *Joint patterns*

The joints are identified by making steep sawtooth cuts in the strata

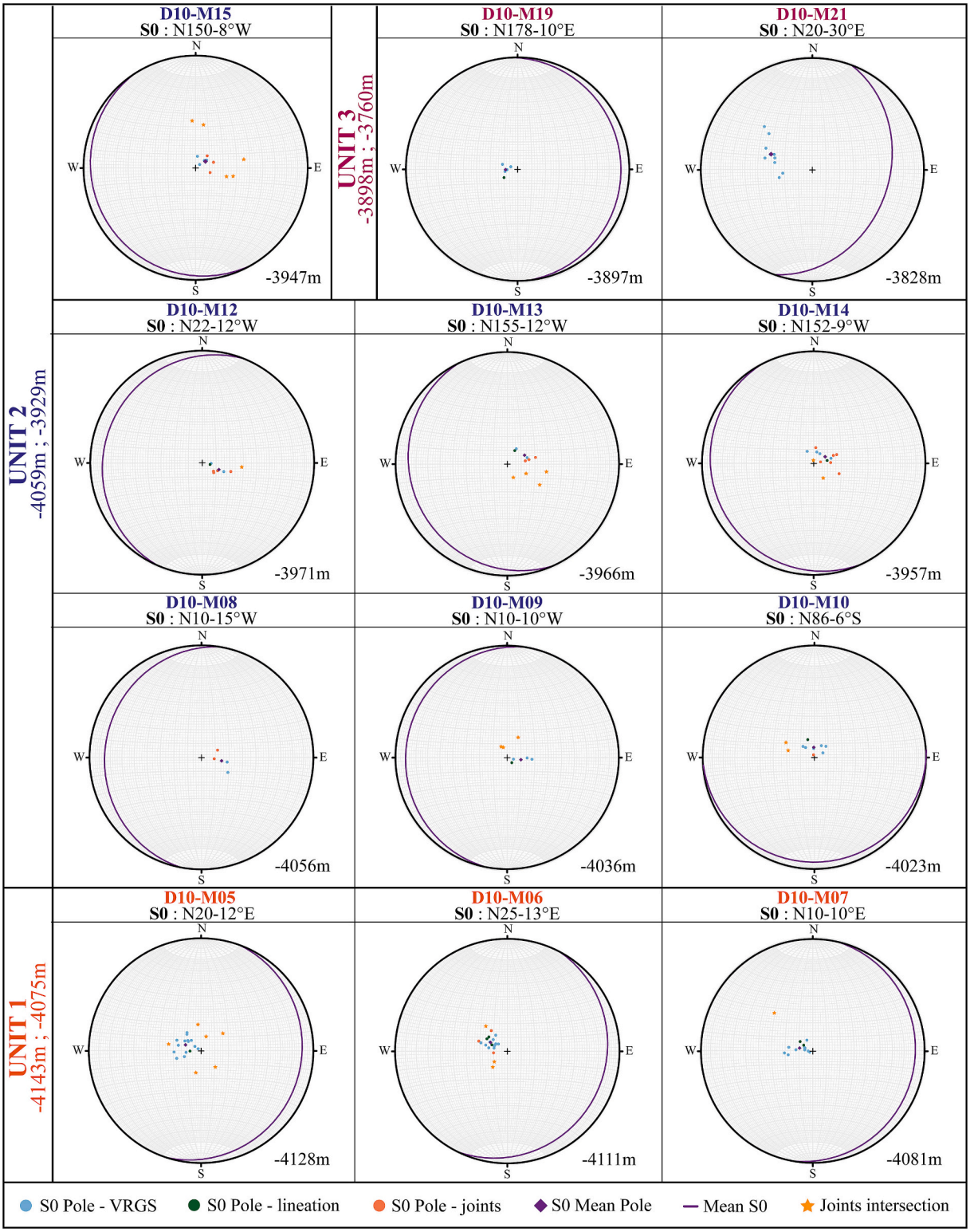

Fig. 8. Compilation of the stereographic projections (on the Schmidt canvas) of the S0 poles obtained, for each zone, with the three measurement methods and the joint intersections. The mean circle represents the calculated mean S0.

boundary (Fig. 10C). The joint system consists of a set of two intersecting joints in each stratum. The intersection of two joints sometimes coincides with the directly measured S0 pole (Fig. 12). In this case, the pole generated by the intersecting joints is almost superimposed on the measured S0 pole, indicating that the joints are perpendicular to the stratification surface. According to this, each pole determined with the intersecting joints is considered as an S0 measurement. As a result, three S0 measurements were added for the first unit and nineteen measurements were added for the second unit (Fig. 8). We also show that joint intersections may not coincide with the measured S0 poles and therefore cannot be considered when determining the mean S0 pole for each outcrop (models D10-M05 to D10-M07 and D10-M09 to D10-M15,

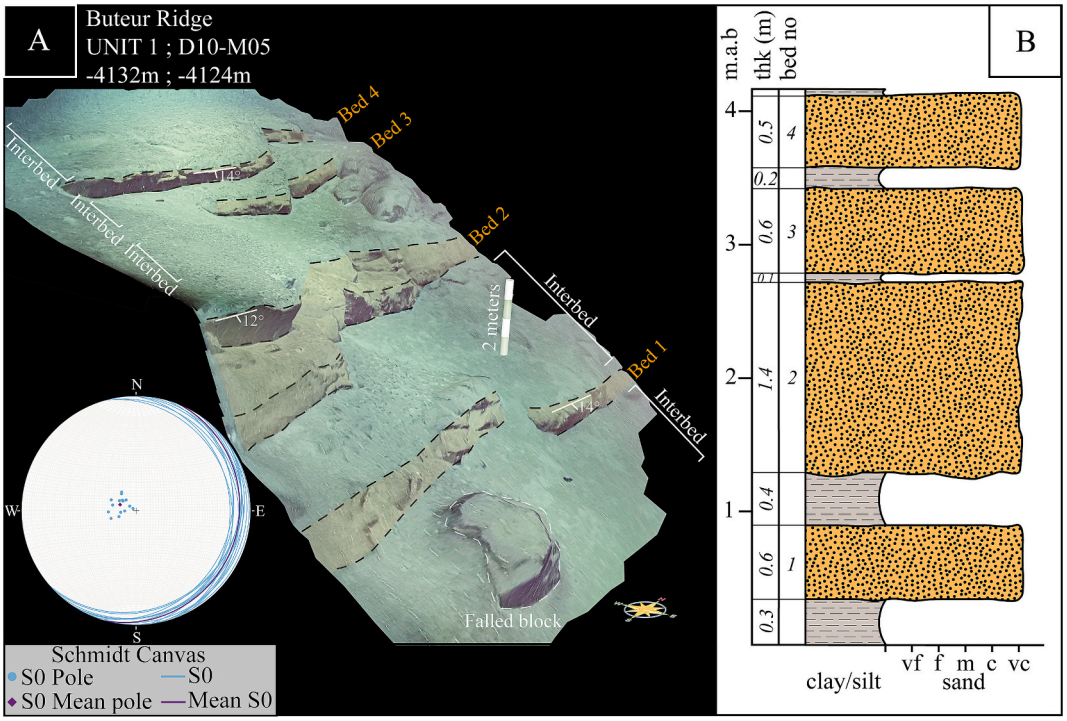

Fig. 9. (A): Illustration of the Unit 1 strata and interbeds morphology using model D10-M05 (Dimensions: ~ 12 m wide, ~ 18 m long and ~ 8 m high) from the *Nautile* dive. The boundaries of the strata are indicated by the dotted black lines. Schmidt canvas showing all the S0 measured (pole and great circle) and the mean S0 calculated (pole and great circle). (B): Sedimentological log based on interpretation of the 3D model. m.a.b: metres above base; thk: thickness.

Fig. 8). The joint sets can be either orthogonal or conjugate, depending on the layer. This is due to the fact that the dihedral angle, which is the angle between the two joint sets, ranges from 65° to 85° (Fig. 12). The presence of systematic joints is evident in the first and second units, but they are more prevalent and form more robust networks in the more competent and thicker beds of the second unit. In contrast, the third unit shows no evidence of joints (Fig. 13).

4.1.3. Rockfalls and collapsed beds

Along the eastern slope of the Buteur Ridge, rockfalls and collapsed beds are observed together with in situ outcrops. Rockfalls are formed by several fallen blocks that have been moved down the slope. It is therefore difficult to know where the fallen blocks originally came from. We interpret collapsed beds as resulting from the winnowing by currents of the underlying interbeds. This winnowing over-erodes the interbed and destabilises the upper bed, causing the collapse. The movement of the collapsed bed is limited and it is easy to restore the original position of the bed.

Large rockfalls are found at the base of the slope (from 4225 to 4150 m below sea level) (Fig. 13). The fallen blocks are mainly metric in size, but can be up to three metres high and four metres wide. Samples N1 and N2 were collected from these rockfalls (Fig. 13). They are fine- to medium-grained, well quartz-cemented sandstones with relatively high iron oxide content. Iron oxidation is only found in the third stratigraphic unit of the Buteur Ridge, which may indicate that these samples originally came from these upper beds.

Three 3D reconstructions show collapsed beds. In particular, D10-M11 shows a large area of highly altered and fractured decimetre-thick beds that are no longer in their stratigraphic position. Sample N7 was taken from this level (Fig. 7) and shows a medium-grained sandstone with poor cementation and containing a large amount of chlorite clay type indicating a high degree of alteration (Fig. 13). Here the low competence due to the low quartz and high clay lithology may have contributed to the collapse of the beds. Collapsed beds are also found in the second unit. In this unit, the large network of joints may have contributed to the collapse.

5. Discussion

5.1. Limitations of the photogrammetric method from the Nautile's video

The primary aim of the *Nautile* dives during the DIADEM cruise was not photogrammetry but rather the sampling and observation of outcrops on the Demerara Plateau. Consequently, the video recordings were not acquired using optimal settings for photogrammetric purposes. The method presented here was developed post-DIADEM cruise to enhance structural measurements.

While other studies have employed photogrammetric techniques for 3D reconstruction in underwater and deep-sea environments (Arnaubec et al., 2023; Escartín et al., 2016; Ferrera et al., 2023; Flores and ten Brink, 2024; Garcia et al., 2017; Gerdes et al., 2019; Kwasnitschka et al., 2013; ten Brink et al., 2023; ten Brink et al., 2024), few have focused on applying structural measurements to inaccessible geological structures. Moreover, very few address the challenges associated with the combined movements of non-fixed horizontal cameras and the underwater vehicle. Flores and ten Brink (2024) acknowledge this limitation, noting that issues with camera orientation arise only when combined with changes in the camera's focal length. However, their study does not record the movements of the cameras. To mitigate this, they assume a fixed value for the camera angle, which introduces additional uncertainty into the photogrammetric results.

In our study, neglecting the combined movements of the cameras and the *Nautile* leads to non-reproducible photogrammetric models. Moreover, the validation of measurements against the photogrammetric models generated by the vertical camera consistently fails. For instance, the strata in the 3D model generated with the horizontal camera appear to be tilted westward, while both the 3D model created with the vertical camera and the direct observations from the scientist aboard indicate the strata are tilted eastward. Therefore, it is crucial to account for the combined effects of both the camera's non-fixed movements and the

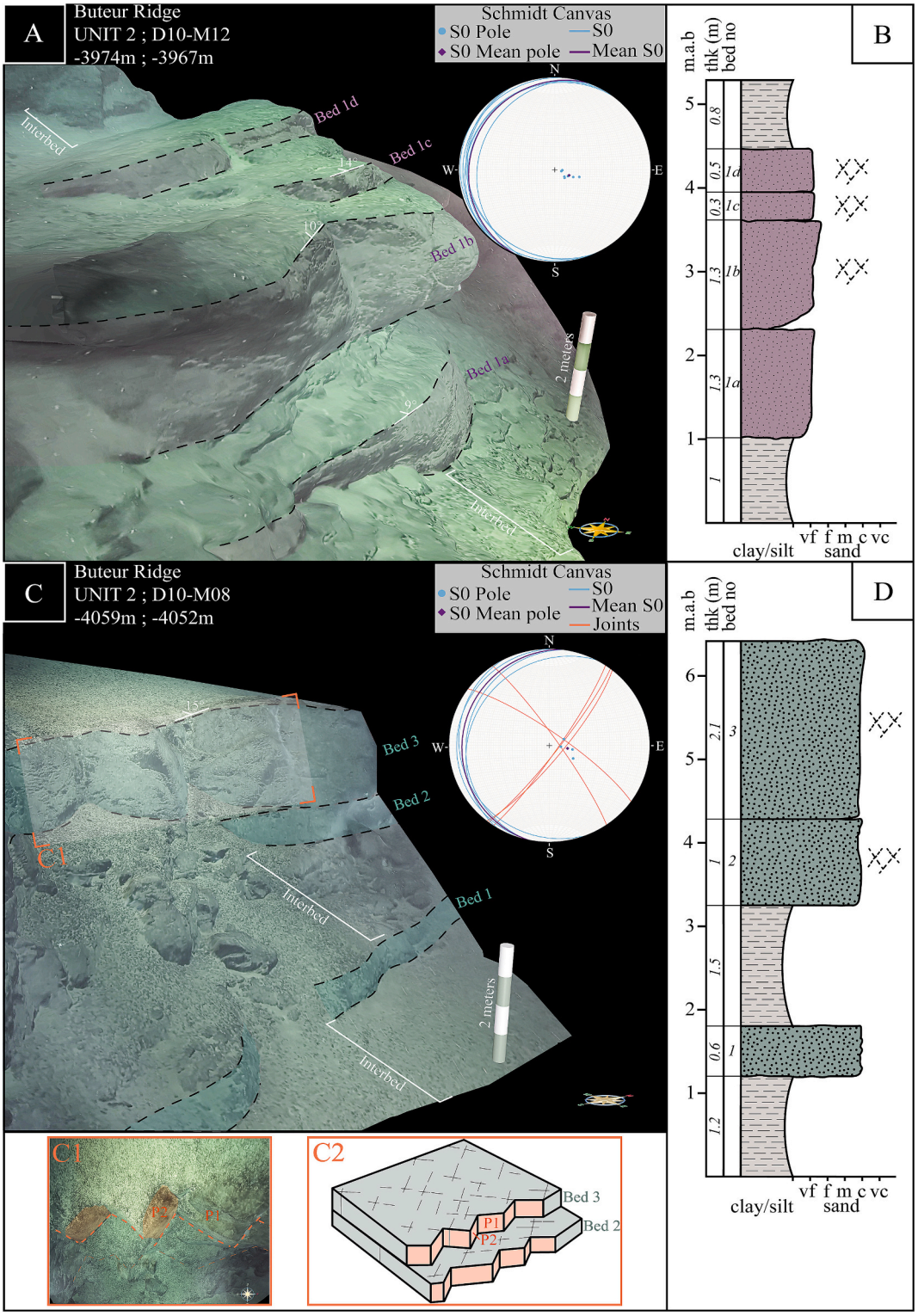

Fig. 10. (A): Illustration of the Unit 2 (upper part) strata and interbeds morphology using model D10-M12 (Dimensions: ~ 14 m wide, ~ 12 m long and ~ 7 m high) from the *Nautile* dive. The boundaries of the strata are indicated by the dotted black lines. Schmidt canvas showing all the S0 measured (pole and great circle) and the mean S0 calculated (pole and great circle) for the model D10-M12. (B): Sedimentological log based on interpretation of the model D10-M12. (C): Illustration of the Unit 2 (lower part) strata, interbeds and joints morphology using model D10-M08 (Dimensions: ~ 9 m wide, ~ 12 m long and ~ 7 m high) from the *Nautile* dive. Schmidt canvas showing all the S0 measured (pole and great circle); the mean S0 calculated (pole and great circle); and the projection of joint sets for the model D10-M08. (C1): Vertical view above the bed showing the joint system. The dotted orange lines highlight the steep sawtooth cuts in the strata boundary. P1: plane 1; P2: plane 2. (C2): Schematic 3D representation of the joint system within two sedimentary beds. (D): Sedimentological log based on interpretation of the model D10-M08. m.a.b: metres above base; thk: thickness.

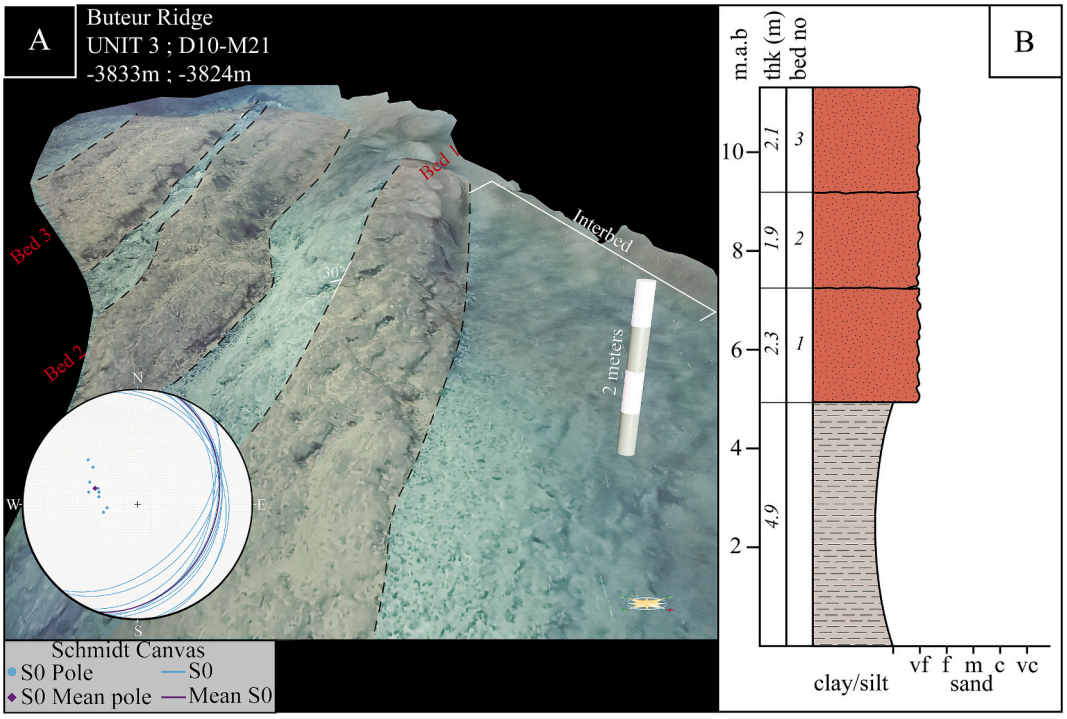

Fig. 11. (A): Illustration of the Unit 3 strata and interbed morphology using model D10-M21 (Dimensions: ~ 11 m wide, ~ 23 m long and ~ 9 m high) from the *Nautile* dive. The boundaries of the strata are indicated by the dotted black lines. Schmidt canvas showing all the S0 measured (pole and great circle) and the mean S0 calculated (pole and great circle). (B): Sedimentological log based on interpretation of the 3D model. m.a.b: metres above base; thk: thickness.

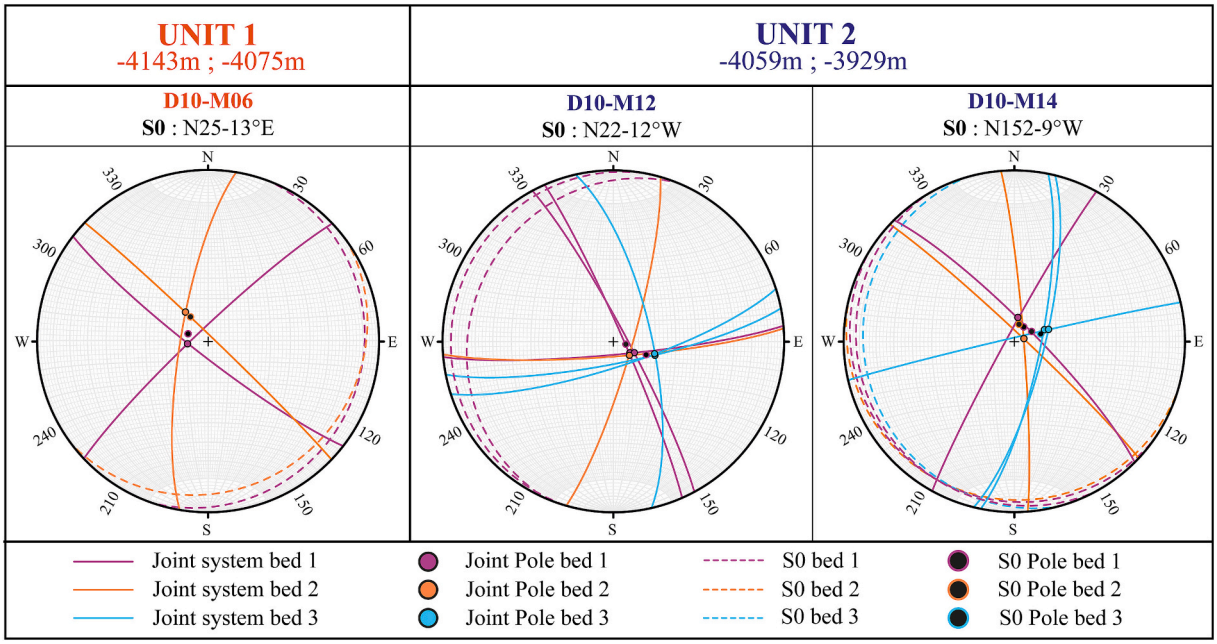

Fig. 12. Stereographic projections (on the Schmidt canvas) of the joint systems for each bed of model D10-M06 (Unit 1) and models D10-M12 and D10-M14 (Unit 2). Comparison of the mean S0 calculated from direct structural measurements using the VRGS © tool (black pole and great circle shown as coloured dotted line) and the S0 obtained from the intersection of the projected joint planes (coloured pole). The angle between the two sets of joints ranges from 65° to 85°.

Nautile's movements.

To address this issue, our study incorporates the recorded movements of the cameras, along with the *Nautile*'s navigation data. Consequently, we use the actual angle of the camera relative to the *Nautile* for each time iteration. This additional correction ensures the systematic validation of models generated with the non-fixed horizontal camera and those produced using conventional photogrammetry methods, where the camera (in this case, vertical) is fixed. Additionally, as proposed by Arnaubec et al. (2023) and Istenič et al. (2019), we utilised the navigation data from the *Nautile*'s INS, which were corrected for drift using the USBL data to enhance the accuracy of the 3D reconstructions.

However, at such depths, several other factors, as mentioned in previous studies (e.g., Arnaubec et al., 2023; Flores and ten Brink, 2024), limit the observations and prevent this protocol from being

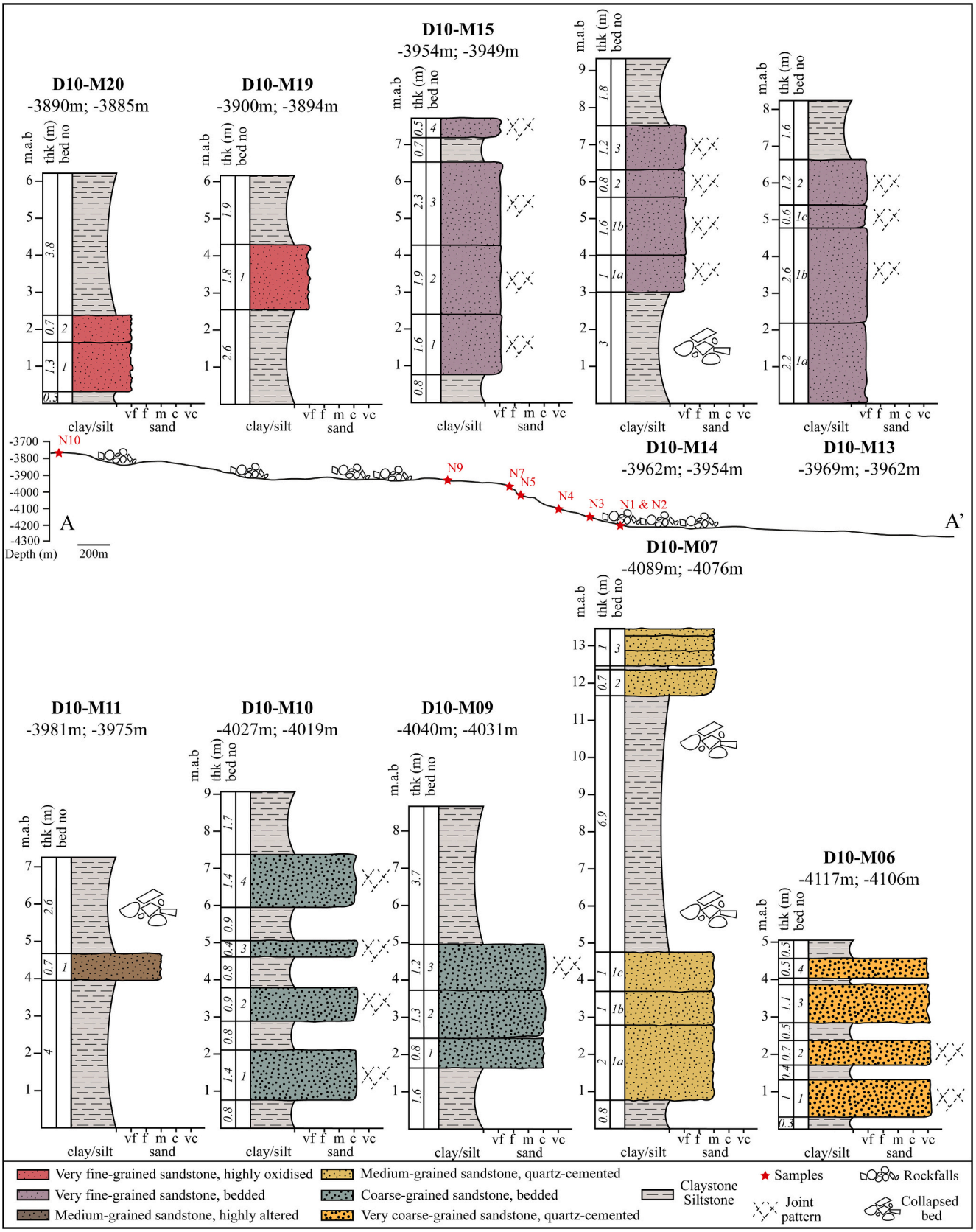

Fig. 13. Compilation of sedimentological logs based on the interpretation of all the 3D reconstructions. The samples and rockfalls are located along the topographic profile (AA') of the *Nautile* dive. See Fig. 1 for location. m.a.b: metres above base; thk: thickness.

applied continuously to the video recording. Among the factors that may affect the quality of photogrammetric reconstructions, the following can be highlighted:

(i) Outcrop distance from the *Nautile* and lighting: a distance of more than ten metres degrades the quality of the video (darkening), while moving too close to the seafloor causes turbidity that obscures the field of view and leads to a backscattering effect (Garcia et al., 2017). We selected navigation areas where the *Nautile* operates close to the outcrops, typically between 2 and 4 m. This proximity helps minimise the blue bias effect on the images and ensures proper illumination of the observed structures. On other hand, as the *Nautile* moves linearly across the outcrop, one-way lighting creates numerous shadow zones behind the structures. If these areas are not illuminated by the *Nautile*'s rotational movement around the structure, they cannot be modelled correctly. The textured meshes are often smoothed around these zones limiting the accuracy of the structure reconstruction. The geological structures used for structural analysis are primarily sedimentary layers, often of metric scale, with clear boundaries. To minimise errors, measurements are taken only in areas where texture effects are minimal (i.e., along edges or on clean surfaces). Arnaubec et al. (2023) and Flores and ten Brink (2024) propose an image pre-processing approach to enhance image quality by correcting contrast and colour distortion. This step helps highlight textures or objects that are otherwise difficult to discern but also increases the quantity and quality of homologous points during point cloud construction, as suggested by Istenič et al. (2019). In our study, we did not apply colour correction, as the resolution obtained during acquisitions is already sufficient to meet the requirements of structural geology. However, this could represent an avenue for improving the method we have followed.

(ii) *Nautile* speed and motion blur: a high speed reduces the number of homologous points between photographs (fewer photographs acquired). The cross-referencing of images during the photogrammetric process is therefore less effective. This results in poorly textured models, which can lead to large measurement errors. Because we use the 1 Hz frequency record of *Nautile* and camera motion data, we cannot improve the resolution by oversampling the video. Istenič et al. (2019) state that to minimise motion blur, it is essential to adjust the survey speed, often to approximately one-quarter of the distance to the scene. The maximum speed of the *Nautile* on the seabed is 1.7 knots (approximately 0.83 $m.s^{-1}$). When navigating close to areas of interest, in our case near the outcrops, the *Nautile* speed is reduced to a minimum, approximately 0.1 $m.s^{-1}$, which satisfy the previous condition. Therefore, in our case, motion blur is primarily caused by the movement of the cameras. As a result, sequences with significant camera movements were excluded from the photogrammetric process. However, in cases where areas of interest contained blurry images after video trimming, these images were manually removed from the sequence. Five photogrammetric blocks required the removal of blurry images during the pre-processing phase. In each block, this involved only one or two images from the entire sequence, resulting in a maximum gap of two seconds. This gap has minimal impact on image continuity, as the reduced speed of the *Nautile* and the absence of significant camera movements in these sequences ensured at least 70 % overlap, which is considered satisfactory as discussed by Arnaubec et al. (2023).

(iii) Camera lens focal length changes: as noted by Flores and ten Brink (2024), the zoom of the HD camera differs from that of the ROV when it operates very close to an object, as zooming changes the peripheral viewing angle at the edges of the image. For the photogrammetry software to function correctly, it is crucial to maintain the camera's apparent focal length as constant as possible, especially when the camera angle is changing. To meet this requirement, we selected video sequences that did not involve any zooming of the camera.

The 3D models generated after taking these constraints into account show acceptable error percentages. Empirically, a structural analysis carried out by simple observation through the submarine's porthole is based on visual estimates by the scientific onboard or from the video record, but without any measuring tools. Therefore, the use of photogrammetry increases the number of geological features that can be orientated, and decreases drastically the uncertainties on the orientation. Here, the error percentages of the measurements are similar to those that could be obtained during a structural field study. In addition, the reproducibility of the measurements taken for each unit allows confidence in the structural observations presented in this paper.

In conclusion, a future improvement for this method in order to reduce the limitations will be the correction of the raw images (e.g., Arnaubec et al., 2023; Flores and ten Brink, 2024; Garcia et al., 2017; Istenič et al., 2019) and a better camera calibration (Li et al., 1997). In addition, it can be proposed to follow the recommendations already presented in Kwasnitschka et al. (2013) for future dives. The submersible should:

(i) Reduce its speed when approaching an outcrop.
(ii) Ensure that the entire outcrop is photographed with the correct lighting. This recommendation assumes that the submersible turns around the outcrop. However, depending on the nature of the outcrop, this may not be possible.
(iii) Do not use zoom lenses when photographing the outcrop and always use 4 K camera mode.

It is important to remember that these recommendations may conflict with other diving objectives (e.g., sampling, maximising distance covered, diving constraints such as strong currents, etc.). However, the photogrammetric method presented in this article shows that it is possible to make the best use of out-of-purpose video records, as well as previous recordings as far as they contain the movements of both underwater device and camera.

5.2. Structure and stratigraphy of the Buteur Ridge

5.2.1. Local variation of the beds dip azimuth and dip direction

Some models, especially models D10-M05 and D10-M06, show a dispersion of the stratification poles centred around the mean pole (Fig. 8). In comparison, several stereographic projections show a distribution of stratification poles fitting a plane (models D10-M07, D10-M09, D10-M10, D10-M14 and D10-M21) (Fig. 8). We consider only the poles determined by direct measurement (S0 determined with the VRGS © tool and the lineation method). As a result, models D10-M08, D10-M12 and D10-M13, whose stratification poles were mainly determined by intersections of joints, do not have enough direct measurement points to determine whether their dispersion is aligned or centred.

The stratification poles of models D10-M07, D10-M09, D10-M10 and D10-M14 fit planes mainly oriented E-W (respectively: N78–4°S; N83–3°N; N100–8°S and N111–8°S). The stratification poles of model D10-M21 show an alignment along a N-S oriented plane (N154–24°E). A first hypothesis for these alignments can be that the topography of outcrops may induce an oriented bias on the measurements. The outcrops topography of models D10-M07 and D10-M14 is oriented E-W, similar to the respective dispersion planes. In contrast, the topography of the other outcrops is not oriented as the dispersion planes. This first hypothesis therefore fails to explain the pole orientations for all models.

Folded structures also show a similar pole alignment (Ramsay et al., 1983). In this hypothesis, the stratigraphic surfaces are measured along the fold flanks. As a result, the change in dip of the stratigraphic surface

is related to the change in distance with the fold axis. However, in several models (D10-M07 and D10-M09) variations in dip do not change in a single direction, as that are not related to depth (multi-metre scale) but occur within a bed at a centimetre scale. Small scale changes in dip do not appear to favour folding deformation.

The detrital sediments deposition in the flow direction can also induce variations in attitude related to hydrodynamics, such as ripple marks or progradation processes. As an example, prograding surfaces occur at different scales (tens of metres to centimetres). At small scales, progradation results in cross-bedding. Similarly, the detrital sediments deposition can induce progradation processes perpendicular to the regional flow direction. For example, the channel levees may be formed by a stack of prograding laminae. These sedimentary structures such as prograding surfaces can result in the alignment of stratigraphic poles at various scales (Crowell, 1955). As the stratigraphic sequence of the Buteur Ridge consists entirely of detrital material (Fig. 7), it is reasonable to assume that the variations in orientation within this clastic system are due to sedimentary processes, such as progradation. These processes are visible both at the scale of a single bed (models D10-M07 and D10-M09) and at the scale of multiple beds (models D10-M10, D10-M14 and D10-M21). Even if the limited number of measurements, and the accuracy of both the models and the structural measurements does not allow us to assess in detail the paleocurrents, the overwhelming predominance of E-W rotation axis is in favour of a N-S-directed flow.

Finding a mean stratification plane that is representative of the stratification plane at the outcrop scale is difficult for models with such pole alignment. If the pole dispersion along the axis is small, the mean stratification plane can be used with caution. However, when the variability of the measurements is high, as is the case for the D10-M21 model, the mean stratification pole is only given as an indication. At the large-scale structure of the Buteur Ridge, it seems risky to consider this mean pole as representative.

5.2.2. *Large-scale structure of the Buteur Ridge*

Previous publications locate an east-dipping fault beneath the eastern basin fill (Graindorge et al., 2022; Museur et al., 2021) as well as

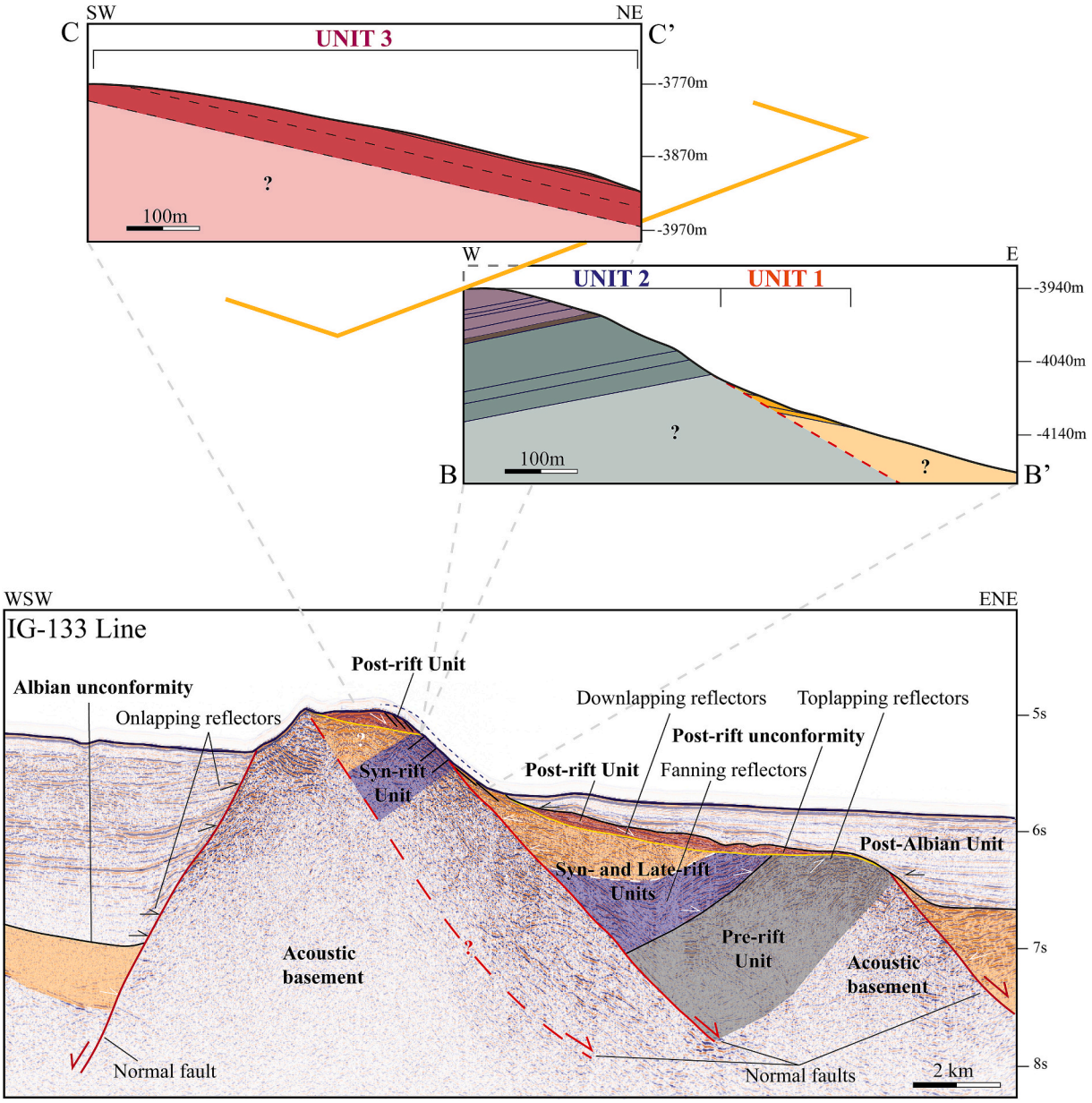

Fig. 14. Combined structural and stratigraphic interpretation of seismic line IG-133 and cross-sections BB' and CC'. No vertical exaggeration for cross-sections, 4.1 for seismic line. See Fig. 1 for locations. Dotted line along the Buteur Ridge flank on seismic line indicate the projected *Nautile* dive path.

a west-dipping fault on the Buteur Ridge western flank (Basile et al., 2022; Girault et al., 2023). These two normal faults can be identified on seismic line IG-133 (Fig. 1C and Fig. 14). The west-dipping fault is identified by the onlapping terminations of low to moderate amplitude seismic reflectors (hanging wall) ending on the acoustic basement (footwall). Beneath the basin fill imaged by flat-lying seismic reflectors, the east-dipping fault is identified as it separates a pack of high amplitude fanning reflectors (at the hanging wall) from the acoustic basement (at the footwall).

In this study, the *Nautile* dive allows structural measurements to be made along the eastern slope of the Buteur Ridge (Fig. 1A, B and Fig. 14). The following discussion will therefore focus on the eastern part of the IG-133 seismic line, between the Buteur Ridge and the easternmost normal fault.

Beneath the filling of the abyssal plain east of the Buteur Ridge, the deepest seismic unit consists of west-dipping high-amplitude seismic reflectors, overlain by eastward onlaps (Fig. 1C and Fig. 14). This second seismic unit consists of medium amplitude fan-shaped reflectors at the base and east-dipping medium amplitude reflectors at the top (Fig. 1C and Fig. 14). These two seismic units are truncated by an unconformity as indicated by the toplapping reflections of the deepest seismic unit (Fig. 1C and Fig. 14). Low-amplitude reflectors onlapping westwards overlain the unconformity. We interpret the deep units as a westward tilted block. The deepest seismic unit may correspond to a pre-rift unit overlain by syn- and late-rift fill (Fig. 14). Both are sealed by an eastward tilted post-rift unconformity (Fig. 14). This tilted block would thus be bounded by an east-dipping normal fault along the eastern flank of the Buteur Ridge as suggested by Basile et al. (2022). However, the fault trace is not clearly identifiable on the seismic line.

Structural analysis of the eastern outcrop has revealed three sedimentary units with different dips. The deepest unit (Unit 1) dips about eleven degrees to the east (Fig. 8). Conversely, the upward second unit dips about ten degrees to the west (Fig. 8). This abrupt change in orientation occurs between 4076 and 4059 m depth on the eastern flank of the Buteur Ridge. We interpret it as the emergence of the normal fault inferred from the seismic line, even if the fault has not been directly observed during the *Nautile* dive. An alternative explanation may be to relate the change in dip to a fold. However, the short distance between the two sedimentary units would require a very tight overfold, and there is no evidence of folding at the outcrop scale, making this fold hypothesis very unlikely.

The Unit 1 dips an average of eleven degrees to the east (Fig. 8). Plotted on seismic line IG-133, the deepest, east-dipping outcrop belongs to the seismic unit lying below the post-rift unconformity, identifying the deep outcropping unit as part of the syn-rift unit (Fig. 14). Upward, the second outcropping unit dips to the west. However, it is difficult to correctly identify west-dipping seismic reflectors on the seismic line. Some very faint reflections towards the west are visible between 5.432 TWTT (two-way travel time) and 5.234 TWTT along the outcrop of the Buteur Ridge (Fig. 1C and Fig. 14). This corresponds to a depth between 4074 and 3925.5 m which is consistent with the observation of the second sedimentary unit (4059–3929 m depth). We tentatively attribute this west-dipping unit to syn-rift sediments, similar to the syn-rift unit of the tilted block observed eastward in the seismic section (Fig. 14). Therefore, given that both Unit 1 and Unit 2 are part of the syn-rift unit, the observed dip variation can be attributed to fault drag structures in Unit 1, where strata near the surface are deformed into folds that are convex in the direction of relative slip (e.g., Brandes and Tanner, 2014; Ferrill et al., 2012; Jackson et al., 2006). In Unit 1, the truncated ends of the dragged layers point away from the direction of the actual relative movement.

This interpretation of the Unit 2 as syn-rift sediments implies that an additional normal fault should be located westward. However, the quality of the seismic line beneath the Buteur Ridge does not allow us to identify seismic evidences for a normal fault. As a result, we can only propose to locate this fault in the acoustic basement of the Buteur Ridge (Fig. 14).

At the top of the Buteur Ridge, the third outcropping sedimentary unit dips about ten degrees to the east (Fig. 8). It is difficult to identify on the seismic line due to the reflection of seismic waves on the sea floor. However, the end of the faint reflectors, tilted to the west, at 5.234 TWTT is consistent with the bottom of the third sedimentary unit at 3898 m depth (Fig. 14).

The abrupt change in orientation between the east-dipping top unit (Unit 3) and the west-dipping intermediate unit (Unit 2) can be geometrically constrained as a surface dipping up to 5° eastward, between sections BB' and CC' (Fig. 14) along the *Nautile* dive path (Fig. 1A). Because the dip of this surface, separating the syn-rift unit from the upper unit, is reminiscent of the dip of the post-rift unconformity in the basin, we similarly interpret the underlying surface as the post-rift unconformity. This east-dipping unconformity surface could appear on the IG-133 seismic line at the top of the Buteur Ridge (Fig. 14). As a result, we interpret the third unit to belong to the post-rift unit (Fig. 14). By plotting the dips of the third sedimentary unit on the seismic line, it appears that the reflectors would then downlap on the post-rift unconformity (Fig. 14). Downlaps would be consistent with sediment progradation, as previously suggested.

Finally, the post-rift unit appears east of the Buteur Ridge as a thin seismic unit, with high amplitude reflectors eastward downlapping. It is overlain by the low amplitude flat-lying reflectors of the basin fill above another unconformity, which merges with the post-rift unconformity further east (Fig. 1C and Fig. 14). It has been referred to previously as the Late Albian unconformity (Basile et al., 2013; Girault et al., 2023; Graindorge et al., 2022; Loncke et al., 2015; Loncke et al., 2020; Loncke et al., 2022; Mercier De Lépinay, 2016; Museur et al., 2021). It therefore appears that the post-rift unconformity and the Late Albian unconformity are indeed two different surfaces, as suggested by Basile et al. (2005, 2013); Sapin et al. (2016) and more recently Fonseca et al. (2024).

Considering the results of the comparative study between the seismic observations of the IG-133 seismic line and the structural observations of the *Nautile* dive, we illustrate the tectonic and stratigraphic evolution of the Buteur Ridge on the five sketches of Fig. 15. The first stage is the deposition of the pre-rift unit, which does not crop out on the eastern flank of the Buteur Ridge. Normal faults then induce two west-dipping tilted blocks, the pre-rift unit tilts to the west, and syn- and late-rift units, partly made of sediments from the first and second outcropping sedimentary units, settle. After this rifting stage, the post-rift unconformity erodes the syn- and late-rift units and truncates the top of the tilted blocks. The post-rift unit, consisting of the third sedimentary unit, then progrades above the post-rift unconformity. Finally, the last event would be a final uplift of the Buteur Ridge block, forming the present relief (Fig. 15). This late and post-rift uplift seems to be associated with normal fault reactivation from the offset of the post-rift unconformity (Fig. 14 and Fig. 15). The normal fault reactivation induces fault drag in the syn-rift unit along the hanging wall, resulting in an eastward dip of the superficial strata, similar to that of the fault. The post-rift uplift and fault reactivation can be related to the lithospheric loading by the Amazon deep-sea fan, which spread east of the Buteur Ridge, and that induced an oceanward flexure of the whole continental margin (Watts et al., 2009).

6. Conclusions

In this study, the use of a new photogrammetric method adapted to *Nautile*'s records allowed the reconstruction of 3D models illustrating most of the sedimentary structures and sequences present on the eastern face of the Buteur Ridge. The use of 3D models allows to overcome the uncertainties associated with visual measurements during a structural study carried out by diving. Without this method, it would have been technically difficult to assess the differences in dip orientation of structures that are almost sub-horizontal. As a result, the structural data

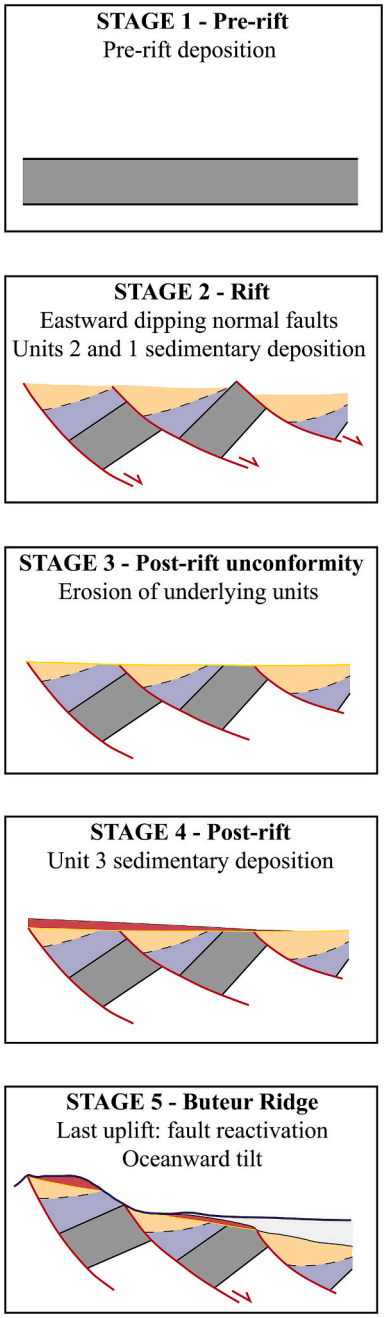

Fig. 15. Reconstruction of the tectonic and stratigraphic events leading to the present relief of the Buteur Ridge. Same vertical exaggeration as the seismic line IG-133.

obtained from the 3D models, combined with seismic observations, allow for the first time to constrain the tectonic events that led to the present relief of the Buteur Ridge, with an initially unexpected accuracy. We interpret these small-scale observations as resulting from tilted blocks overlapped by a post-rift unit. The post-rift unconformity has subsequently been offset by the later fault reactivation. In addition, sampling carried out during the *Nautile* dive revealed that the eastern flank of the Buteur Ridge is entirely made up of clastic rocks. Combining these data with structural measurements, it was even possible to highlight the progradation of the sedimentary fills.

The underwater photogrammetry method presented in this article can be used either for past video recordings or either for future submarine dives. The only condition for using this method is to know both the camera movements and the movements of the submarine equipment. Although the development of this method was used here to carry out a detailed structural and stratigraphic geological study, it can subsequently be used in other scientific fields.

Supplementary data to this article can be found online at https://doi.org/10.1016/j.margeo.2025.107609.

CRediT authorship contribution statement

Charline Coudun: Writing – review & editing, Writing – original draft, Formal analysis. **Paul Brichard:** Methodology. **Christophe Basile:** Writing – review & editing, Supervision, Funding acquisition. **Sébastien Zaragosi:** Writing – review & editing, Methodology, Conceptualization. **Vincent Marieu:** Writing – review & editing, Methodology, Conceptualization. **Martin Patriat:** Writing – review & editing, Investigation. **Lies Loncke:** Writing – review & editing, Funding acquisition.

Funding

This work was supported by grants from Ifremer, ISTerre, LabEx OSUG@2020 and CNRS-INSU to Christophe Basile.

Declaration of Competing Interest

The authors declare the following financial interests/personal relationships which may be considered as potential competing interests:

Christophe Basile reports financial support was provided by IFREMER. Christophe Basile reports financial support was provided by ISTerre. Christophe Basile reports financial support was provided by LabEx OSUG. Christophe Basile reports financial support was provided by CNRS. If there are other authors, they declare that they have no known competing financial interests or personal relationships that could have appeared to influence the work reported in this paper.

Acknowledgments

We thank the French Oceanographic Fleet (FOF) for access to the *Pourquoi Pas?* research vessel and equipment used in this study. We would also like to thank the crew of the *Pourquoi Pas?* for the optimal conditions in which the DIADEM mission took place. We thank the *Nautile* crew for all the technical information. We also thank the captains and crews of the Research Vessels *L'Atalante* and *Pourquoi Pas?* for data acquisition during the surveys IGUANES, DRADEM, MARGATS. We would like to thank Uri ten Brink and the two anonymous reviewers for their insightful and constructive feedback.

Data availability

The public datasets are available in the following repertories: IGUANES cruise (doi: 10.17600/13010030); DRADEM cruise (doi: 10.17600/16001900); MARGATS cruise (doi: 10.17600/16001400); DIADEM cruise (doi: 10.17600/18000672). All other supplementary data supporting the findings of this study are available on request from the corresponding author.

References

Agisoft, L.L.C., 2022. *Agisoft Metashape* (version 2.0.0). Available online (accessed on 25 March 2025). https://www.agisoft.com.

Allmendinger, R.W., 2024. *Stéréonet* (version 11.6.0). Available online (accessed on 25 March 2025). https://www.rickallmendinger.net/stereonet.

Arnaubec, A., Ferrera, M., Escartín, J., Matabos, M., Gracias, N., Opderbecke, J., 2023. Underwater 3D Reconstruction from Video or still Imagery: Matisse and 3DMetrics Processing and Exploitation Software. J. Mar. Sci. Eng. 11, 985. https://doi.org/10.3390/jmse11050985.

Basile, C., 2016. DRADEM cruise, RV Pourquoi pas ? https://doi.org/10.17600/16001900.

Basile, C., Loncke, L., 2023. DIADEM cruise, RV Pourquoi pas ? https://doi.org/10.17600/18000672.
Basile, C., Mascle, J., Guiraud, R., 2005. Phanerozoic geological evolution of the Equatorial Atlantic domain. J. Afr. Earth Sci. 43, 275–282. https://doi.org/10.1016/j.jafrearsci.2005.07.011.
Basile, C., Maillard, A., Patriat, M., Gaullier, V., Loncke, L., Roest, W., Mercier De Lépinay, M., Pattier, F., 2013. Structure and evolution of the Demerara Plateau, offshore French Guiana: Rifting, tectonic inversion and post-rift tilting at transform–divergent margins intersection. Tectonophysics 591, 16–29. https://doi.org/10.1016/j.tecto.2012.01.010.
Basile, C., Loncke, L., Roest, W.R., Graindorge, D., Klingelhoefer, F., Museur, T., Heuret, A., Lesourd-Laux, T., Vetel, W., 2022. Initiation of transform continental margins: the cretaceous margins of the Demerara plateau. Geol. Soc. Spec. Publ. 524, 327–337. https://doi.org/10.1144/SP524-2021-118.
Bemis, S.P., Micklethwaite, S., Turner, D., James, M.R., Akciz, S., Thiele, S.T., Bangash, H.A., 2014. Ground-based and UAV-Based photogrammetry: a multi-scale, high-resolution mapping tool for structural geology and paleoseismology. J. Struct. Geol. 69, 163–178. https://doi.org/10.1016/j.jsg.2014.10.007.
Brandes, C., Tanner, D.C., 2014. Fault-related folding: a review of kinematic models and their application. Earth Sci. Rev. 138, 352–370. https://doi.org/10.1016/j.earscirev.2014.06.008.
ten Brink, U.S., Chaytor, J.D., Flores, C.H., Detmer, S., Wei, Y., Lucas, L.C., Andrews, B. D., Georgiopoulou, A., 2023. Seafloor observations eliminate a landslide as the source of the 1918 Puerto Rico tsunami. Bull. Seismol. Soc. Am. 113, 268–280. https://doi.org/10.1785/0120220146.
ten Brink, U.S., Bialik, O.M., Chaytor, J.D., Flores, C.H., Purkey Phillips, M., 2024. Field geology under the sea with a remotely operated vehicle: Mona Rift, Puerto Rico. Geosphere 20 (6), 1575–1597. https://doi.org/10.31223/X5Z69K.
Campan, A., 1995. Analyse cinématique de l'Atlantique équatorial : implications sur l'évolution de l'Atlantique Sud et sur la frontière de plaques Amérique du Nord/Amérique du Sud. Thesis. 352p. Université Pierre et Marie Curie. https://theses.fr/1995PA066555.
Chesley, J.T., Leier, A.L., White, S., Torres, R., 2017. Using unmanned aerial vehicles and structure-from-motion photogrammetry to characterize sedimentary outcrops: an example from the Morrison Formation, Utah, USA. Sediment. Geol. 354, 1–8. https://doi.org/10.1016/j.sedgeo.2017.03.013.
Crowell, J.C., 1955. Directional-current structures from the prealpine flysch, Switzerland. GSA Bull. 11 (66), 1351–1384. https://doi.org/10.1130/0016-7606(1955)66[1351:DSFTPF]2.0.CO;2.
Escartín, J., Leclerc, F., Olive, J.-A., Mevel, C., Cannat, M., Petersen, S., Augustin, N., Feuillet, N., Deplus, C., Bezos, A., et al., 2016. First Direct Observation of Coseismic Slip and Seafloor Rupture along a Submarine Normal Fault and Implications for Fault Slip history. Earth Planet. Sci. Lett. 450, 96–107. https://doi.org/10.1016/j.epsl.2016.06.024.
Esri, 2025. *ArcGIS Pro* (version 3.4.3). Available online. https://www.esri.com/en-us/arcgis/products/arcgis-pro (accessed on 25 March 2025).
Ferrera, M., Arnaubec, A., Boittiaux, C., Larroche, I., Opderbecke, J., 2023. Vision-based 3D Reconstruction for Deep-Sea Environments: Practical Use for surveys and Inspection. In: Presented at the OCEANS 2023 - Limerick, IEEE, Limerick, Ireland, pp. 1–7. https://doi.org/10.1109/OCEANSLimerick52467.2023.10244338.
Ferrill, D.A., Morris, A.P., McGinnis, R.N., 2012. Extensional fault-propagation folding in mechanically layered rocks: the case against the frictional drag mechanism. Tectonophysics 576–577, 78–85. https://doi.org/10.1016/j.tecto.2012.05.023.
Flores, C.H., ten Brink, U.S., 2024. Photogrammetry of the Deep Seafloor from Archived Unmanned Submersible Exploration Dives. J. Mar. Sci. Eng. 12, 1250. https://doi.org/10.3390/jmse12081250.
Fonseca, J.C., Ranero, C.R., Vannucchi, P., Iacopini, D., Vital, H., 2024. The Tectonic Structure and Evolution of the Potiguar-Ceará Rifted margin of Brazil. Tectonics 43, e2023TC008184. https://doi.org/10.1029/2023TC008184.
Garcia, R., Gracias, N., Nicosevici, T., Prados, R., Hurtos, N., Campos, R., Escartin, J., Elibol, A., Hegedus, R., 2017. Exploring the Seafloor with Underwater Robot. In: Computer Vision in Vehicle Technology: Land, Sea and Air, 1. https://doi.org/10.1002/9781118868065, 10.1002/9781118868065.ch4.
Gerdes, K., Martínez Arbizu, P., Schwarz-Schampera, U., Schwentner, M., Kihara, T.C., 2019. Detailed Mapping of Hydrothermal Vent Fauna: a 3D Reconstruction Approach based on Video Imagery. Front. Mar. Sci. 6, 96. https://doi.org/10.3389/fmars.2019.00096.
Girault, I., Basile, C., Bernet, M., Paquette, J., Heuret, A., Loncke, L., Poetisi, E., Balvay, M., 2023. Thermochronology and U–Pb dating of detrital zircons from the Demerara Plateau (French Guiana-Suriname): Implications for the provenance of the Early Cretaceous syn-rift sedimentation. Basin Res. 35, 1386–1406. https://doi.org/10.1111/bre.12758.
Gonçalves, J.A., Henriques, R., 2015. UAV photogrammetry for topographic monitoring of coastal areas. ISPRS J. Photogramm. Remote Sens. 104, 101–111. https://doi.org/10.1016/j.isprsjprs.2015.02.009.
Gouyet, S., 1988. Evolution tectono-sédimentaire des marges guyanaise et nord-brésilienne au cours de l'ouverture de l'Atlantique Sud. Thesis. 374p.. Université de Pau.
Graindorge, D., Klingelhoefer, F., 2016. MARGATS cruise. RV L'Atalante. https://doi.org/10.17600/16001400.
Graindorge, D., Museur, T., Klingelhoefer, F., Roest, W.R., Basile, C., Loncke, L., Sapin, F., Heuret, A., Perrot, J., Marcaillou, B., Lebrun, J.F., Déverchère, J., 2022. Deep structure of the Demerara Plateau and its two-fold tectonic evolution: from a volcanic margin to a transform marginal plateau, insights from the Conjugate Guinea Plateau. Geol. Soc. Spec. Publ. 524, 339–366. https://doi.org/10.1144/SP524-2021-96.
Greenroyd, C.J., Peirce, C., Rodger, M., Watts, A.B., Hobbs, R.W., 2008. Do fracture zones define continental margin segmentation? — evidence from the French Guiana margin. Earth Planet. Sci. Lett. 272, 553–566. https://doi.org/10.1016/j.epsl.2008.05.022.
Hartley, R.I., Zisserman, A., 2004. Multiple View Geometry in Computer Vision, 2nd ed. Cambridge University Press, Cambridge, UK. ISBN 0521540518.
Honarmand, M., Shahriari, H., 2021. Geological Mapping using Drone-based Photogrammetry: an Application for Exploration of Vein-Type Cu Mineralization. Minerals 11, 585. https://doi.org/10.3390/min11060585.
ImageMagick Studio, L.L.C., 2018. *ImageMagick* (version 7). Available online (accessed on 25 March 2025). https://imagemagick.org.
Istenič, K., Gracias, N., Arnaubec, A., Escartín, J., Garcia, R., 2019. Scale Accuracy Evaluation of Image-based 3D Reconstruction strategies using Laser Photogrammetry. Remote Sens. 11, 2093. https://doi.org/10.3390/rs11182093.
Jackson, C.A.L., Gawthorpe, R.L., Sharp, I.R., 2006. Style and sequence of deformation during extensional fault-propagation folding: examples from the Hammam Faraun and El-Qaa fault blocks, Suez Rift, Egypt. J. Struct. Geol. 28, 519–535. https://doi.org/10.1016/j.jsg.2005.11.009.
Jiménez-Jiménez, S.I., Ojeda-Bustamante, W., Marcial-Pablo, M., Enciso, J., 2021. Digital Terrain Models Generated with Low-cost UAV Photogrammetry: Methodology and Accuracy. ISPRS Int. J. Geo Inf. 10, 285. https://doi.org/10.3390/ijgi10050285.
Kwasnitschka, T., Hansteen, T.H., Devey, C.W., Kutterolf, S., 2013. Doing fieldwork on the seafloor: Photogrammetric techniques to yield 3D visual models from ROV video. Comput. Geosci. 52, 218–226. https://doi.org/10.1016/j.cageo.2012.10.008.
Le Suave, R., Beuzart, P., 2003. GUYAPLAC cruise, RV L'Atalante. https://doi.org/10.17600/3010050.
Li, R., Li, H., Zou, W., Smith, R.G., Curran, T.A., 1997. Quantitative photogrammetric analysis of digital underwater video imagery. IEEE J. Ocean. Eng. 22, 364–375. https://doi.org/10.1109/48.585955.
Liang, B., Liu, Y., Su, Z., Zhang, N., Li, S., Feng, W., 2023. A Workflow for Interpretation of Fracture Characteristics based on Digital Outcrop Models: a Case Study on Ebian XianFeng Profile in Sichuan Basin. Lithosphere 2022, 7456300. https://doi.org/10.2113/2022/7456300.
Loncke, L., 2013. IGUANES cruise, RV L'Atalante. https://doi.org/10.17600/13010030.
Loncke, L., Maillard, A., Basile, C., Roest, W.R., Bayon, G., Gaullier, V., Pattier, F., Mercier De Lépinay, M., Grall, C., Droz, L., Marsset, T., Giresse, P., Caprais, J.C., Cathalot, C., Graindorge, D., Heuret, A., Lebrun, J.F., Bermell, S., Marcaillou, B., Sotin, C., Hebert, B., Patriat, M., Bassetti, M.A., Tallobre, C., Buscail, R., Durrieu De Madron, X., Bourrin, F., 2015. Structure of the Demerara passive-transform margin and associated sedimentary processes. Initial results from the IGUANES cruise. Geol. Soc. Spec. Publ. 431, 179–197. https://doi.org/10.1144/SP431.7.
Loncke, L., Roest, W.R., Klingelhoefer, F., Basile, C., Graindorge, D., Heuret, A., Marcaillou, B., Museur, T., Fanget, A.S., Mercier De Lépinay, M., 2020. Transform marginal Plateaus. Earth Sci. Rev. 203, 102940. https://doi.org/10.1016/j.earscirev.2019.102940.
Loncke, L., Mercier De Lépinay, M., Basile, C., Maillard, A., Roest, W.R., De Clarens, P., Patriat, M., Gaullier, V., Klingelhoefer, F., Graindorge, D., Sapin, F., 2022. Compared structure and evolution of the conjugate Demerara and Guinea transform marginal plateaus. Tectonophysics 822, 229112. https://doi.org/10.1016/j.tecto.2021.229112.
Loparev, A., Rouby, D., Chardon, D., Dall'Asta, M., Sapin, F., Bajolet, F., Ye, J., Paquet, F., 2021. Superimposed Rifting at the Junction of the Central and Equatorial Atlantic: Formation of the Passive margin of the Guiana Shield. Tectonics 40, e2020TC006159. https://doi.org/10.1029/2020TC006159.
Luhmann, T., Fraser, C., Maas, H.-G., 2015. Sensor modelling and camera calibration for close-range photogrammetry. ISPRS J. Photogramm. Remote Sens. 115, 37–46. https://doi.org/10.1016/j.isprsjprs.2015.10.006.
Mercier De Lépinay, M., 2016. Inventaire mondial des marges transformantes et évolution tectonosédimentaire des plateaux de Demerara et de Guinée. Thesis. 335p.. Université de Perpignan, Université de Perpignan Via Domitia, Perpignan https://theses.fr/2016PERP0004.
Mercier De Lépinay, M., Loncke, L., Basile, C., Roest, W.R., Patriat, M., Maillard, A., De Clarens, P., 2016. Transform continental margins – part 2: a worldwide review. Tectonophysics 693, 96–115. https://doi.org/10.1016/j.tecto.2016.05.038.
Mozas-Calvache, A.T., Pérez-García, J.L., Cardenal-Escarcena, F.J., Mata-Castro, E., Delgado-García, J., 2012. Method for photogrammetric surveying of archaeological sites with light aerial platforms. J. Archaeol. Sci. 39, 521–530. https://doi.org/10.1016/j.jas.2011.10.007.
Museur, T., Graindorge, D., Klingelhoefer, F., Roest, W.R., Basile, C., Loncke, L., Sapin, F., 2021. Deep structure of the Demerara Plateau: from a volcanic margin to a Transform marginal Plateau. Tectonophysics 803, 228645. https://doi.org/10.1016/j.tecto.2020.228645.
Nemčok, M., Rybár, S., Ekkertová, P., Kotulová, J., Hermeston, S.A., Jones, D., 2015. Transform-margin model of hydrocarbon migration: the Guyana–Suriname case study. Geol. Soc. Spec. Publ. 431, 199–217. https://doi.org/10.1144/SP431.6.
Peace, A.L., Jess, S., 2023. Microdrones in field-based structural geology: a photogrammetry and fracture quantification case study from the North Mountain Basalt, Nova Scotia, Canada. Drone Syst. Appl. 11, 1–15. https://doi.org/10.1139/dsa-2022-0037.
Ramsay, J.G., Huber, M.I., Lisle, R.J., 1983. The Techniques of Modern Structural Geology: Folds and Fractures. Academic Press, 0125769229, 9780125769228. 391p.
Ryan, J.C., Hubbard, A.L., Box, J.E., Todd, J., Christoffersen, P., Carr, J.R., Holt, T.O., Snooke, N., 2015. UAV photogrammetry and structure from motion to assess calving dynamics at Store Glacier, a large outlet draining the Greenland ice sheet. Cryosphere 9, 1–11. https://doi.org/10.5194/tc-9-1-2015.

Sangsrichan, K., Manopkawee, P., Kanthata, S., 2023. 3D Digital Outcrop Model for Geological Structure Analysis in Mae Moh Coal Mine, Lampang Province, Thailand. Int. J. Geoinform. 19. https://doi.org/10.52939/ijg.v19i9.2847.

Sapin, F., Davaux, M., Dall'asta, M., Lahmi, M., Baudot, G., Ringenbach, J.-C., 2016. Post-rift subsidence of the French Guiana hyper-oblique margin: from rift-inherited subsidence to Amazon deposition effect. Geol. Soc. Spec. Publ. 431, 125–144. https://doi.org/10.1144/SP431.11.

Serifoglu Yilmaz, C., Gungor, O., 2016. Comparison of the performances of ground filtering algorithms and DTM generation from a UAV-based point cloud. Geocarto Int. 33, 522–537. https://doi.org/10.1080/10106049.2016.1265599.

Serifoglu Yilmaz, C., Yilmaz, V., Güngör, O., 2018. Investigating the performances of commercial and non-commercial software for ground filtering of UAV-based point clouds. Int. J. Remote Sens. 39, 5016–5042. https://doi.org/10.1080/01431161.2017.1420942.

Śledź, S., Ewertowski, M.W., Piekarczyk, J., 2021. Applications of unmanned aerial vehicle (UAV) surveys and Structure from Motion photogrammetry in glacial and periglacial geomorphology. Geomorphology 378, 107620. https://doi.org/10.1016/j.geomorph.2021.107620.

Sona, G., Pinto, L., Pagliari, D., Passoni, D., Gini, R., 2014. Experimental analysis of different software packages for orientation and digital surface modelling from UAV images. Earth Sci. Inf. 7, 97–107. https://doi.org/10.1007/s12145-013-0142-2.

Svennevig, K., Guarnieri, P., Stemmerik, L., 2015. From oblique photogrammetry to a 3D model – Structural modeling of Kilen, eastern North Greenland. Comput. Geosci. 83, 120–126. https://doi.org/10.1016/j.cageo.2015.07.008.

Ventura, D., Bonifazi, A., Gravina, M.F., Belluscio, A., Ardizzone, G., 2018. Mapping and Classification of Ecologically Sensitive Marine Habitats using Unmanned Aerial Vehicle (UAV) Imagery and Object-based image Analysis (OBIA). Remote Sens. 10, 1331. https://doi.org/10.3390/rs10091331.

Vollgger, S.A., Cruden, A.R., 2016. Mapping folds and fractures in basement and cover rocks using UAV photogrammetry, Cape Liptrap and Cape Paterson, Victoria, Australia. J. Struct. Geol. 85, 168–187. https://doi.org/10.1016/j.jsg.2016.02.012.

VRGeoscience Limited, 2022. *Virtual reality Geological Studio (VRGS)* (version 3.1). Available online (accessed on 25 March 2025). https://www.vrgeoscience.com.

Wang, Y., 1998. Principles and applications of structural image matching. ISPRS J. Photogramm. Remote Sens. 53, 154–165. https://doi.org/10.1016/S0924-2716(98)00002-1.

Watts, A.B., Rodger, M., Peirce, C., Greenroyd, C.J., Hobbs, R.W., 2009. Seismic structure, gravity anomalies, and flexure of the Amazon continental margin, NE Brazil. J. Geophys. Res. 114, B07103. https://doi.org/10.1029/2008JB006259.

Westoby, M.J., Brasington, J., Glasser, N.F., Hambrey, M.J., Reynolds, J.M., 2012. 'Structure-from-Motion' photogrammetry: a low-cost, effective tool for geoscience applications. Geomorphology 179, 300–314. https://doi.org/10.1016/j.geomorph.2012.08.021.

Zhou, Y., Rupnik, E., Meynard, C., Thom, C., Pierrot-Deseilligny, M., 2019. Simulation and Analysis of Photogrammetric UAV image Blocks—Influence of Camera Calibration Error. Remote Sens. 12, 22. https://doi.org/10.3390/rs12010022.